

Rotational multimaterial printing of filaments with subvoxel control

<https://doi.org/10.1038/s41586-022-05490-7>

Received: 16 January 2022

Accepted: 27 October 2022

Published online: 18 January 2023

 Check for updates

Natalie M. Larson^{1,2}, Jochen Mueller^{1,2}, Alex Chortos^{1,2}, Zoey S. Davidson^{1,2}, David R. Clarke¹ & Jennifer A. Lewis^{1,2}✉

Helical structures are ubiquitous in nature and impart unique mechanical properties and multifunctionality¹. So far, synthetic architectures that mimic these natural systems have been fabricated by winding, twisting and braiding of individual filaments^{1–7}, microfluidics^{8,9}, self-shaping^{1,10–13} and printing methods^{14–17}. However, those fabrication methods are unable to simultaneously create and pattern multimaterial, helically architected filaments with subvoxel control in arbitrary two-dimensional (2D) and three-dimensional (3D) motifs from a broad range of materials. Towards this goal, both multimaterial^{18–23} and rotational²⁴ 3D printing of architected filaments have recently been reported; however, the integration of these two capabilities has yet to be realized. Here we report a rotational multimaterial 3D printing (RM-3DP) platform that enables subvoxel control over the local orientation of azimuthally heterogeneous architected filaments. By continuously rotating a multimaterial nozzle with a controlled ratio of angular-to-translational velocity, we have created helical filaments with programmable helix angle, layer thickness and interfacial area between several materials within a given cylindrical voxel. Using this integrated method, we have fabricated functional artificial muscles composed of helical dielectric elastomer actuators with high fidelity and individually addressable conductive helical channels embedded within a dielectric elastomer matrix. We have also fabricated hierarchical lattices comprising architected helical struts containing stiff springs within a compliant matrix. Our additive-manufacturing platform opens new avenues to generating multifunctional architected matter in bioinspired motifs.

Helical architectures that exhibit unique functionalities are abundant in both natural and synthetic systems^{1,2}. For example, the helical assembly of actin and tropomyosin in skeletal muscle thin filaments gives rise to the high contractility and specific work of skeletal muscles^{1,25}. Meanwhile, the nastic motion of plants arises from helically arranged stiff cellulose fibres within plant cell walls^{1,2,17,26–28}. In synthetic systems, recent efforts have focused on creating helical architectures for applications ranging from artificial muscles^{1,3,7,10,29,30} to mechanical metamaterials^{31,32} to hierarchical lattices with rope-like beams¹⁴. Inspired by these helically structured systems, we developed RM-3DP to enable simultaneous fabrication and patterning of multimaterial architected filaments with locally programmable subvoxel control over the orientation of azimuthally heterogeneous features, thus enabling fabrication of synthetic multimaterial helical filaments patterned in arbitrary one-dimensional (1D), 2D and 3D motifs.

Our RM-3DP method combines two enabling features: (1) a multimaterial nozzle with azimuthally heterogeneous subvoxel features and (2) a printhead design that allows several pressure-controlled ink reservoirs as well as the nozzle to rotate freely (Fig. 1a,b). Our nozzles possess a ‘shell–fan–core’ geometry, in which the fan elements generate

an azimuthally heterogeneous architecture (Fig. 1b and Extended Data Fig. 1). Free rotation of the pressure-controlled ink reservoirs and nozzle is enabled by a four-channel rotary union, which transfers pressurized air from a set of stationary inlets to a corresponding set of rotating outlets (see Fig. 1a, Supplementary Video 1 and Methods). The ink reservoirs and nozzle are connected to a shaft, which is coupled to a stepper motor that controls the rotation and angular velocity, ω , of the rotating components of the system. This system is mounted on a three-axis, motion-controlled stage that controls translational velocity, v , and gap height, h , between the printing nozzle and substrate. During printing of helically architected filaments, the ratio of angular to translational velocity, ω/v , determines the shear field and, ultimately, the theoretical helical angle, $\phi(r) = \tan^{-1}(r\omega/v)$, of the multimaterial features embedded within these filaments as a function of radial position r ($r = 0$ at the core centre)²⁴. Mathematically, the ideal interfaces between multimaterial features are helicoidal surfaces. We define a dimensionless rotation rate, $\omega^* = R\omega/v$ (in radians), in which R is the radius of the largest internal nozzle feature, as a measure of the maximum idealized shear field imposed by nozzle rotation and translation during printing²⁴. We also define two more dimensionless parameters: a dimensionless

¹Harvard John A. Paulson School of Engineering and Applied Sciences, Harvard University, Cambridge, MA, USA. ²Wyss Institute for Biologically Inspired Engineering, Harvard University, Cambridge, MA, USA. ✉e-mail: jalewis@seas.harvard.edu

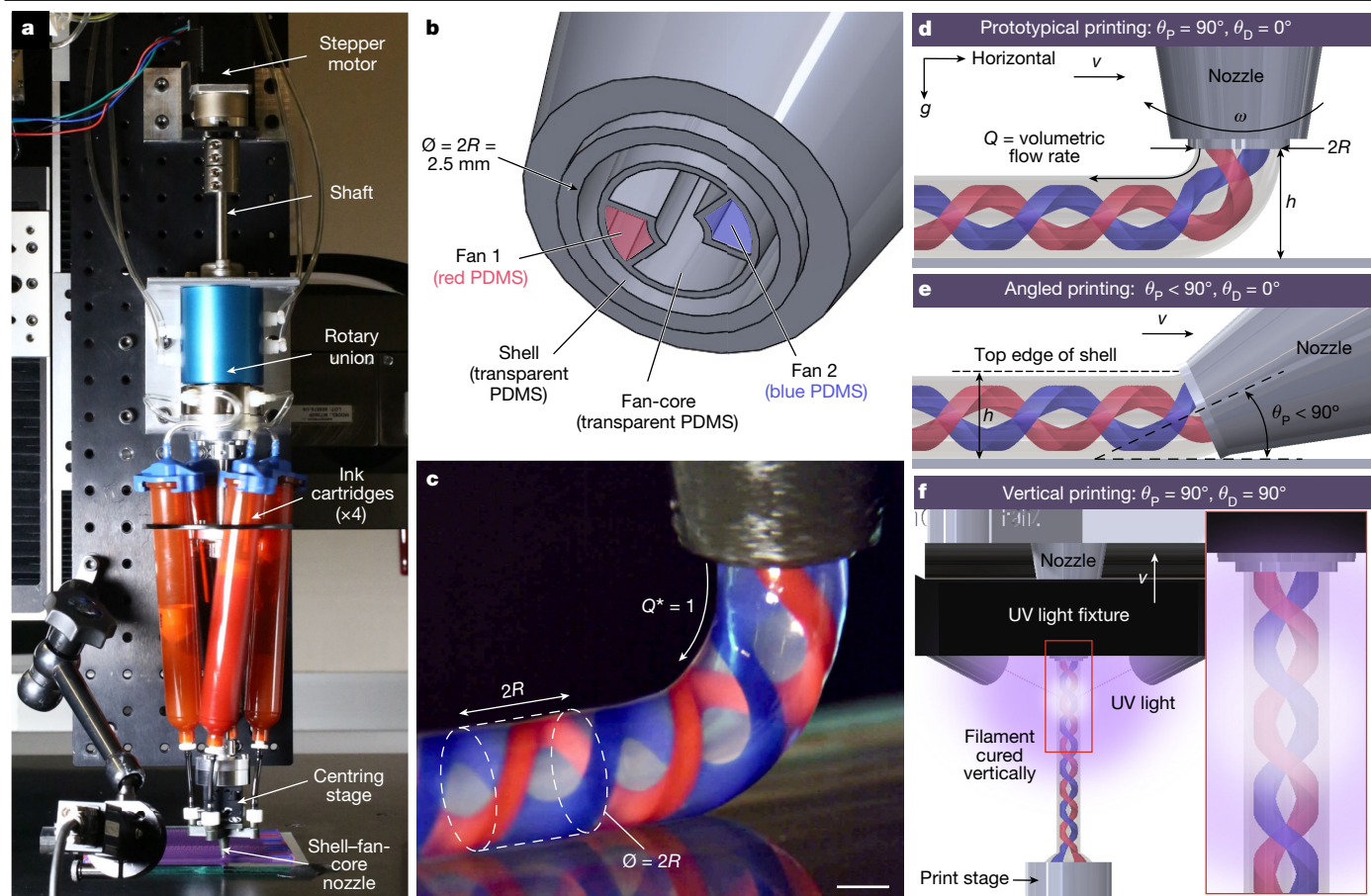


Fig. 1 | Rotational multimaterial 3D printing of architected filaments with programmable subvoxel control. **a**, Image of RM-3DP printhead oriented vertically ($\theta_p = 90^\circ$) and deposition surface oriented horizontally ($\theta_D = 0^\circ$). **b**, 3D model of four-material shell-fan-core nozzle tip (for RM-3DP with $\theta_p = 90^\circ$, $\theta_D = 0^\circ$) with diameter $2R = 2.5$ mm. **c**, Photograph of four-material PDMS filament deposition using the nozzle illustrated in **b**. Print parameters were

$\theta_p = 90^\circ$, $\theta_D = 0^\circ$, $\omega^* = 2$, $Q^* = 1$, $h^* = 2$, $v = 1$ mm s $^{-1}$. A cylindrical voxel is outlined by the dashed white lines. Scale bar, 1 mm. **d–f**, Schematics of three RM-3DP print configurations demonstrated in this work: prototypical printing: $\theta_p = 90^\circ$, $\theta_D = 0^\circ$ (**d**); angled printing: $\theta_p < 90^\circ$, $\theta_D = 0^\circ$ (**e**); vertical printing: $\theta_p = 90^\circ$, $\theta_D = 90^\circ$ (**f**). In **f**, a fixture holds four evenly spaced UV light guides directed at the filament to enable curing on the fly.

gap height, $h^* = h/(2R)$, and a dimensionless volumetric flow rate, $Q^* = Q/(\omega\pi R^2)$, in which Q is the sum of the flow rates Q_i for each channel. Q^* is equal to 1 when the filament radius is equal to the nozzle radius.

Our RM-3DP platform can be used in three configurations (Fig. 1d–f). Each configuration is specified by the angles of the printhead rotation axis (θ_p) and filament deposition (θ_D) relative to the horizontal. Prototypical extrusion-based 3D printing is defined by $\theta_p = 90^\circ$ and $\theta_D = 0^\circ$ (ref. ³³) (Fig. 1d). Meanwhile, angled printing is defined by $\theta_p < 90^\circ$ and $\theta_D = 0^\circ$, in which the gap height, h , now corresponds to the vertical distance between the substrate and the top edge of the shell or outermost nozzle feature (Fig. 1e and Supplementary Video 2). Finally, in vertical printing ($\theta_p = 90^\circ$ and $\theta_D = 90^\circ$), filaments are printed out of plane by translating the nozzle in the z direction (Fig. 1f). To impart mechanical stability to the vertically patterned filaments, the printhead is outfitted with ultraviolet (UV) lights to enable curing on the fly¹⁶.

Printed filament and subvoxel geometries are influenced by the printhead configuration (θ_p and θ_D) as well as ω^* , h^* and Q^* , as demonstrated by a parameter sweep of these conditions using viscoelastic polydimethylsiloxane (PDMS) inks as an example (Figs. 1b and 2a and Extended Data Figs. 2 and 3a,b). The target filament geometry is a subvoxelated^{24,34} straight cylinder with a circular cross-section, in which the volume of an individual voxel for $Q^* = 1$ is defined as $2\pi R^3$ where the voxel length along the filament axis is $2R$ (Fig. 1c). The target subvoxel geometry comprises perfectly helical fan traces that appear

as sinusoidal curves from any view perpendicular to the long axis of the filaments. During prototypical printing ($\theta_p = 90^\circ$, $\theta_D = 0^\circ$), high values of h^* and ω^* lead to instabilities that cause the filaments to become non-cylindrical or deviate from the printhead travel path, similar to those that arise at large h^* in prototypical extrusion-based 3D printing^{35,36}. At the subvoxel level, red and blue fan traces show a warped helical architecture in which the degree of warping becomes increasingly prominent at high ω^* and low h^* . We posit that warping arises in part owing to non-uniform forces around the azimuth of the filament that are inherent to its deposition and relaxation on a substrate and in part to the need for the filament to bend 90° after it exits the nozzle. For particularly low values of h^* (for example, $h^* = 1$), the 90° bend occurs over a relatively short vertical distance, leading to pronounced subvoxel warping. Warping effects induced by filament bending during printing are notably reduced when the printhead is oriented at a shallow angle relative to the deposition surface (for example, $\theta_p = 25^\circ$, $\theta_D = 0^\circ$). For angled printing, optimal filament and subvoxel geometries are observed for $h^* = 1$. However, some degree of subvoxel warping is inherent to printing on a substrate. When needed, vertical printing ($\theta_p = 90^\circ$, $\theta_D = 90^\circ$) can be used to simultaneously eliminate the warping effects caused by the substrate and the bending of the filament.

To further demonstrate the ability to locally program the orientation of subvoxelated filaments on the fly, we printed 1D filaments with gradients in ω^* , switching in ω^* and alternating chirality (Fig. 2b and

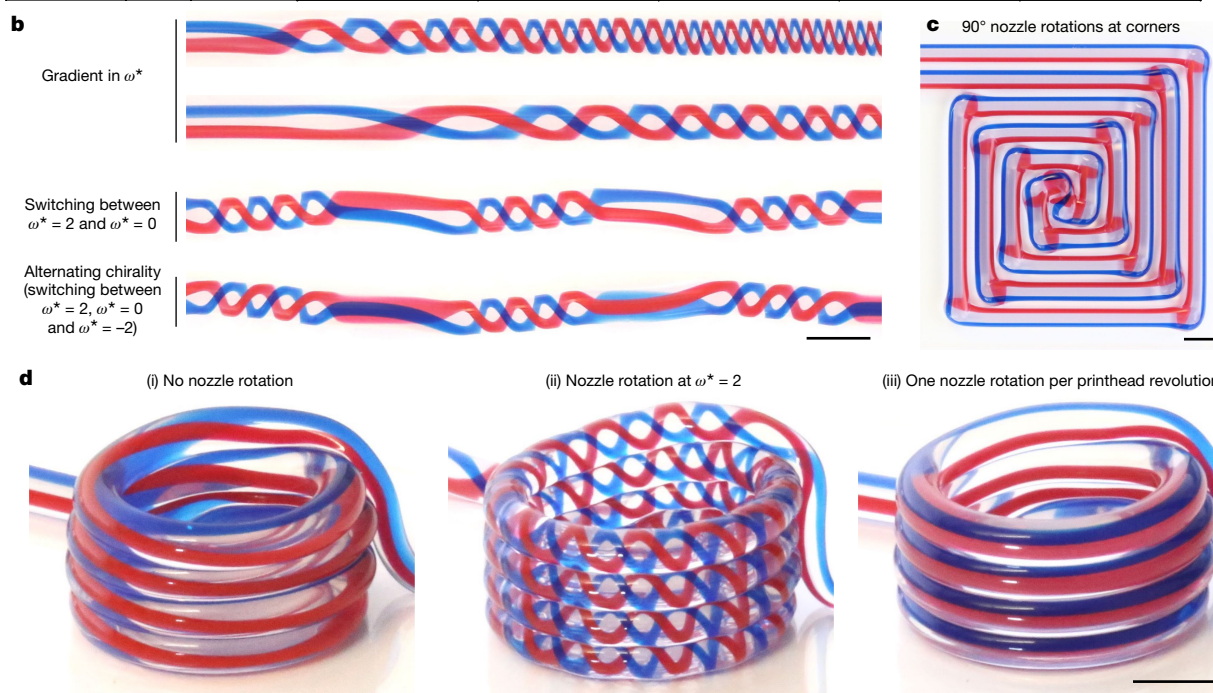
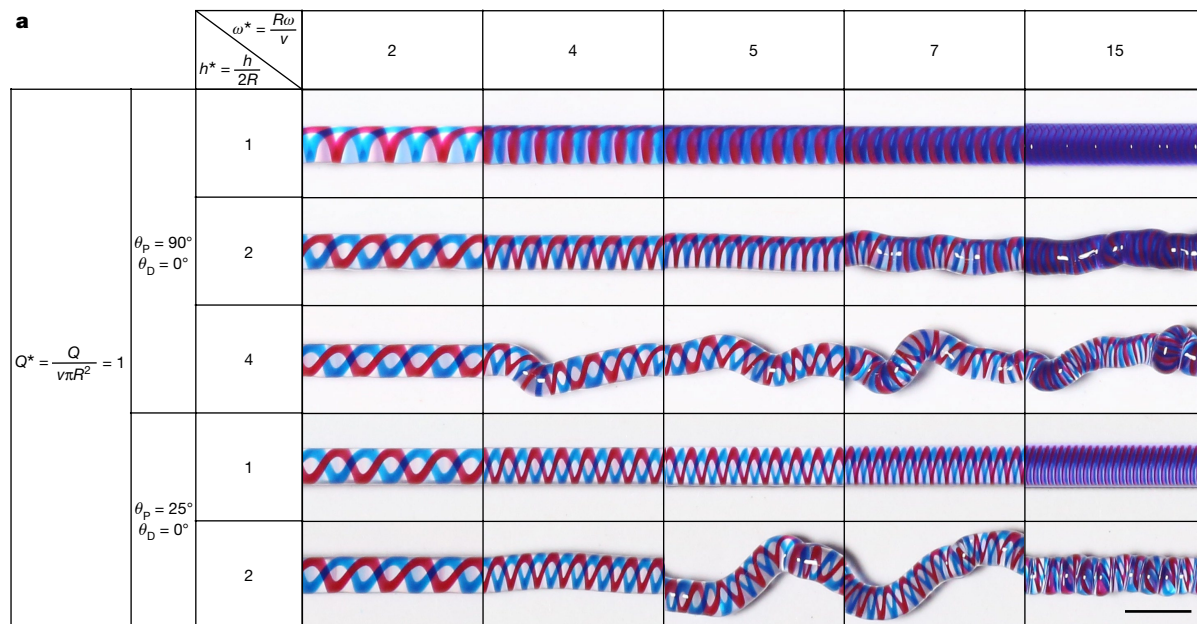


Fig. 2 | Patterning geometric complexity across scales. PDMS filaments extruded from shell–fan–core nozzles presented in Fig. 1b and Extended Data Fig. 1. **a**, Filaments printed at varying values of ω^* , h^* and θ_p (with constant $\theta_D = 0^\circ$ and $Q^* = 1$). **b**, Patterning 1D filaments with gradients in ω^* (rows 1 and 2), switching in ω^* (row 3) and alternating chirality (row 4). Print parameters were $\theta_p = 25^\circ$, $\theta_D = 0^\circ$, $Q^* = 1$, $h^* = 1$, $v = 2 \text{ mm s}^{-1}$. **c**, A 2D square spiral pattern with 90°

printhead rotations at the corners to ensure blue remained on the outside of the trace. Print parameters were $\theta_p = 90^\circ$, $\theta_D = 0^\circ$, $Q^* = 1$, $h^* = 1.1$, $v = 4 \text{ mm s}^{-1}$. **d**, 3D helical print patterns with: (i) no nozzle rotation, (ii) nozzle rotation at $\omega^* = 2$ and (iii) one nozzle rotation per printhead revolution. Print parameters were $\theta_p = 90^\circ$, $\theta_D = 0^\circ$, $Q^* = 1$, $h^* = 2$, $v = 4 \text{ mm s}^{-1}$. All scale bars, 5 mm.

Supplementary Video 3). Further capabilities are highlighted in a 2D square spiral pattern produced by rotating the printhead at discrete locations (that is, only at the corners) to maintain the continuity and location of a given material (shown in blue) along the outside of the filaments within this pattern (Fig. 2c and Supplementary Video 4). In another demonstration, we used a helical print path (Fig. 2d and Supplementary Video 5). Without nozzle rotation (Fig. 2d (i)), we have limited capabilities. However, with nozzle rotation, a hierarchical helical structure with $\omega^* = 2$ (Fig. 2d (ii)) and a helix with the blue fan trace maintained along the outside of the helix superstructure (Fig. 2d (iii)) can be readily fabricated.

Helical dielectric elastomer actuators

To demonstrate our ability to fabricate functional filaments, we designed and printed helical dielectric elastomer actuator (HDEA) filaments with discrete, individually addressable helical conductive channels with high helix angle, thin layers and high multimaterial interfacial area embedded within a dielectric elastomer matrix. The HDEA filaments consist of basic units of actuation composed of soft dielectric elastomer membranes sandwiched between two soft electrodes. HDEAs can be designed to exhibit a contractile response when electrostatic forces compress the dielectric elastomer membranes between helically

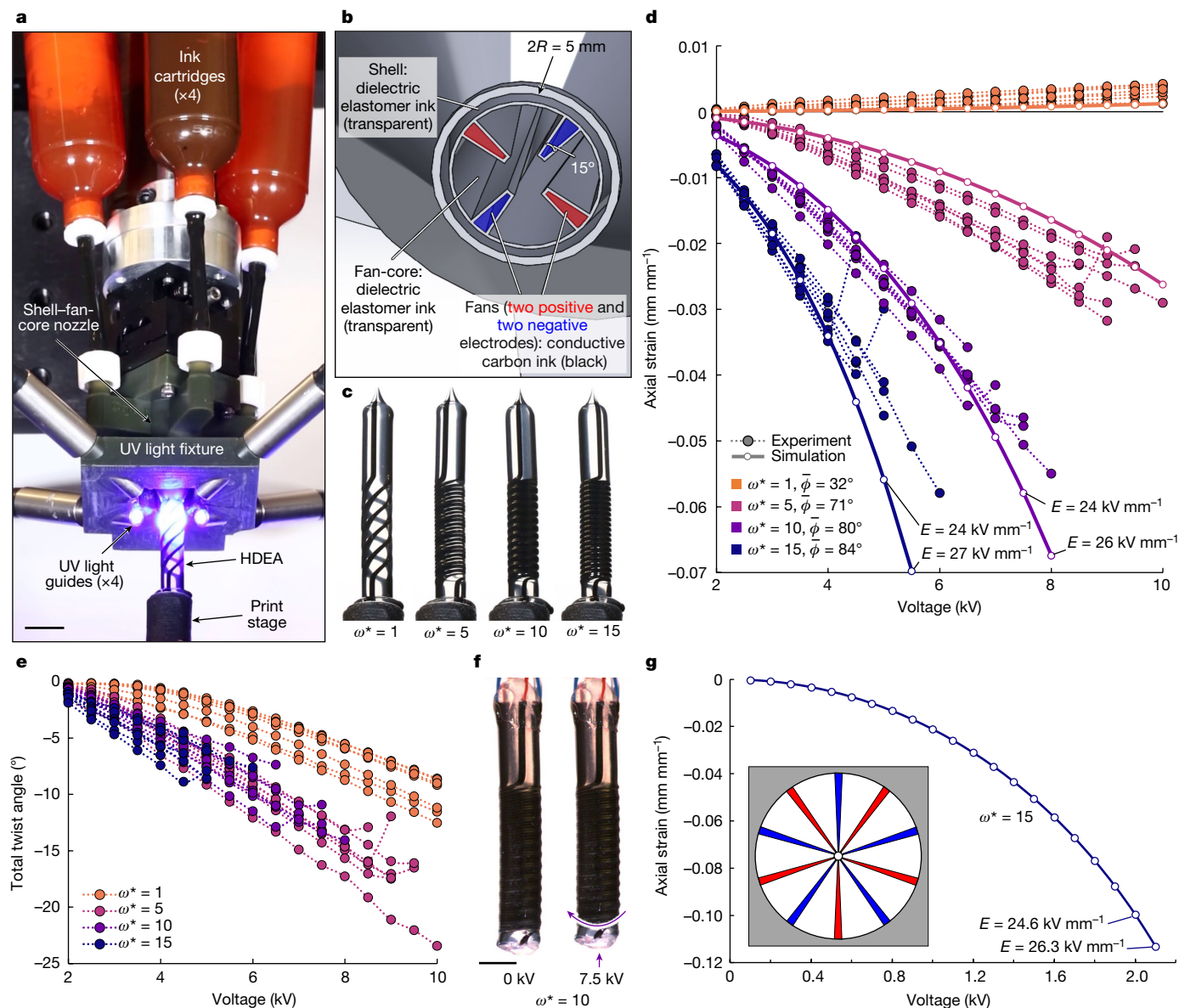


Fig. 3 | HDEA filaments. **a**, Photograph of RM-3DP of an HDEA with $\omega^* = 1$ using the vertical printing ($\theta_p = 90^\circ$, $\theta_b = 90^\circ$) configuration with UV curing on the fly. Scale bar, 10 mm. **b**, 3D model of shell-fan-core nozzle tip. **c**, Photographs of representative filaments with $\omega^* = 1, 5, 10$ and 15 on the print stage immediately after printing. **d**, Experimental and simulated axial actuation strain as a function of voltage for HDEAs with $\omega^* = 1, 5, 10$ and 15 . Theoretical average helical angles over the entire active area, $\bar{\phi}$, are also noted on the plot. For each ω^* , $N = 7$ specimens were tested. For the simulation results, estimated electric fields, E , are noted for the two highest voltage results for $\omega^* = 10$ and 15 . In this and subsequent plots of axial actuation strain, a negative strain means that the

filaments contract axially with applied voltage. **e**, Total twist angle for the entire 20-mm actuator as a function of voltage for each specimen plotted in **d**. A negative twist angle corresponds to a tightening of the helix. **f**, Photograph showing axial contraction and twisting of an HDEA with $\omega^* = 10$. Scale bar, 5 mm. **g**, Simulation results for an HDEA with $\omega^* = 15$, filament diameter = 5 mm, core diameter = 0.25 mm, shell thickness = 0 mm (shell inner diameter = 5 mm) and ten fans with a fan angle of 5° (dielectric volume fraction 0.86). Estimated electric fields are noted for the two highest voltage results. The inset shows a schematic of the simulated filament cross-section.

patterned electrodes. Others have produced HDEAs by helical cutting of a dielectric elastomer tube, deposition of compliant electrodes on the helix faces and device assembly³⁰. Using RM-3DP, HDEAs can be rapidly printed in a single step by co-extruding two viscoelastic inks from a shell-fan-core nozzle to simultaneously form both dielectric (shell, fan-core) and conductive (fans) components in a helical geometry (Fig. 3a–c and Extended Data Fig. 3c,d). The dielectric elastomer components are composed of a soft acrylic ink that, after UV curing, exhibits a Young's modulus $Y_{\text{soft}} = 0.52 \pm 0.03$ MPa (mean \pm standard deviation (s.d.)) and a dielectric constant of 5.45 ± 0.08 (mean \pm s.d.) at 1 kHz (Extended Data Figs. 4a and 5a,b). The conductive ink contains

carbon black particles as a filler, remains as an uncured viscoelastic electrode embedded within the HDEAs and has a conductivity of $8 \times 10^{-3} \pm 2 \times 10^{-3}$ S m^{-1} (mean \pm standard error) at 1 kHz (Extended Data Fig. 5c).

HDEA filaments are fabricated by vertical printing (Figs. 1f and 3a and Supplementary Video 6) using a 5-mm-diameter shell-fan-core nozzle (Fig. 3b and Extended Data Fig. 5d,e) and UV curing on the fly. This approach was ultimately adopted to ensure that the printed filaments have a symmetric subvoxel helical architecture and, hence, display only axial actuation and twisting under an applied voltage. By contrast, HDEA filaments printed at an angle ($\theta_p = 15^\circ$, $\theta_b = 0^\circ$) undergo

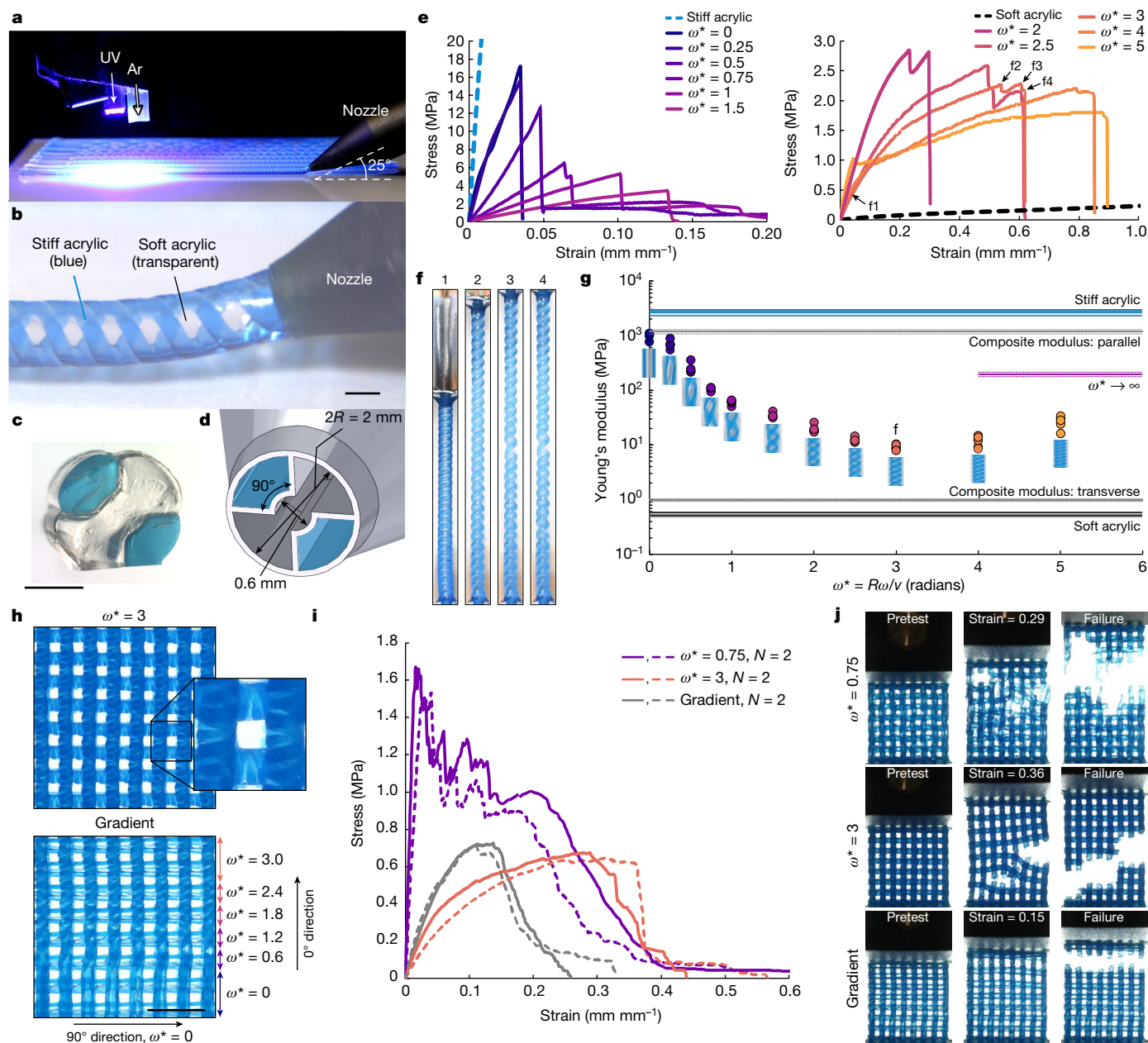


Fig. 4 | Springy filaments and lattices. **a**, RM-3DP of springy filaments using angled configuration with UV curing on the fly under flowing argon. **b**, Springy filament deposition with $\omega^* = 1$. Scale bar, 1 mm. **c**, Springy filament cross-section. Scale bar, 1 mm. **d**, 3D model of fan-core nozzle tip. **e**, Representative stress–strain curves from tensile measurements on springy filaments and soft and stiff acrylic base materials. **f**, Images of tensile testing of springy filament with $\omega^* = 3$. Stress–strain results for this filament are plotted in **e**, with arrows indicating the strain value for each of the four images in **f**. **g**, Young’s modulus of springy filaments as a function of ω^* (circular points; $N = 5$ for each ω^*). Photographs of representative filaments are shown. Young’s moduli of stiff ($N = 9$) and soft ($N = 17$) acrylic base materials are shown as thin solid blue and dark grey lines, respectively. Purple solid and dashed lines

represent the mean \pm s.d. of the theoretical parallel composite modulus, $Y_{\omega^* \rightarrow \infty}$ of a filament with a soft acrylic core and a fan region comprising fully mixed stiff and soft acrylic inks. Grey solid and dashed lines represent the mean \pm s.d. of the theoretical parallel (Y_{\parallel}) and transverse (Y_{\perp}) composite moduli, which represent theoretical upper and lower bounds, respectively, for the springy filament moduli. **h**, Springy lattices composed of springy filaments with $\omega^* = 3$ (top) and with a gradient in ω^* (bottom). Scale bar, 10 mm. **i**, Stress–strain curves from tensile measurements of springy lattices with $\omega^* = 0.75$, $\omega^* = 3$ and a gradient in ω^* for $N = 2$ specimens each (solid and dashed lines). **j**, Images of tensile testing of springy lattices taken before testing (pretest), at an intermediate strain and after failure. The lattices shown here correspond to the stress–strain curves plotted as solid lines in **i**.

warping in their helical structure, which induces a bending response in addition to axial and twisting actuation (Extended Data Fig. 6 and Supplementary Video 7).

HDEA filaments with programmable actuation behaviour are achieved by varying ω^* from 1 to 15 during vertical printing. These filaments are tested in 0.5-kV increments starting at 2 kV applied voltage and increasing up to 10 kV or until electrical breakdown (Fig. 3c–f,

Extended Data Fig. 7, Supplementary Fig. 1a and Supplementary Video 8). The filaments show maximum contractile (negative-valued) strains of about $-4.4 \pm 0.6\%$ (mean \pm s.d., number of specimens $N = 7$) for $\omega^* = 10$ and $-4.1 \pm 0.9\%$ (mean \pm s.d., $N = 7$) for $\omega^* = 15$ (Fig. 3d). Notably, the filaments show contractile strains for $\omega^* = 5, 10$ and 15 and extensile strains for $\omega^* = 1$. The transition from contractile to extensile strains is expected to occur when the helical angle drops below 45° .

Our results are consistent with this prediction, as the theoretical average helical angle over the entire active area, ϕ , decreases from 71° at $\omega^* = 5$ to 32° at $\omega^* = 1$ (Fig. 3d). Meanwhile, all HDEAs, regardless of ω^* , twist in the direction that corresponds to a tightening of the helix (defined as a negative twist angle) (Fig. 3e,f). In applications in which twisting is undesirable, HDEAs with periodically alternating chirality may be designed such that their local twisting opposes the neighbouring twist without affecting the overall achievable axial strain.

We note that RM-3DP could be used to print HDEA filaments with higher actuation strains and lower actuation voltages by implementing more extreme shell–fan–core features (for example, smaller fan angle). To explore this design space, we carried out finite element simulations to predict the axial strain of filaments generated using different feature geometries and a constant filament diameter of 5 mm (see Supplementary Information). For model validation and optimization, simulations are first performed using the same geometries and ω^* values as the above experiments (Fig. 3d and Supplementary Figs. 1b, 2 and 3). Simulations investigating individual geometric parameters (such as core diameter) predict improved performance for geometries with a larger relative dielectric elastomer actuator active area (thinner shell, smaller core), thinner dielectric layers (more fans) and higher dielectric volume fraction (smaller fan angles) (Supplementary Figs. 4–8). A strategic combination of these four parameters could give rise to substantial improvements in HDEA performance. For example, for the geometry shown in Fig. 3g, a contractile strain of ~10% is predicted for $\omega^* = 15$ at an applied voltage of 2 kV (Supplementary Fig. 9). Looking ahead, we plan to generate HDEAs with improved actuation performance using nozzle designs with more extreme features, as well as other functional architectures with high-fidelity helical and orientable channels that are uniquely enabled by RM-3DP.

‘Springy’ filaments and lattices

To generate structural composites, we printed architected ‘springy’ filaments and 3D lattices composed of stiff and soft subvoxelated elements. Springy filaments are fabricated by co-extruding two viscoelastic inks from a fan–core nozzle to embed stiff acrylic springs (blue fan features) within a soft acrylic matrix (transparent fan–core feature) (Fig. 4a–d, Extended Data Figs. 3e,f and 4d,e and Supplementary Video 9). UV curing on the fly is used to minimize interdiffusion between the inks as they come into contact after exiting the nozzle (Fig. 4a–d and Supplementary Video 9). After curing, the Young’s moduli (Y) of the stiff and soft acrylic base materials differ by more than three orders of magnitude: $Y_{\text{stiff}} = 2,700 \pm 200$ MPa and $Y_{\text{soft}} = 0.52 \pm 0.03$ MPa (mean \pm s.d.) (Extended Data Fig. 4a,b).

Notably, we find that the tensile mechanical behaviour of springy filaments can be tuned by varying ω^* (Fig. 4e–g, Extended Data Fig. 8a–k and Supplementary Video 10). As ω^* increases from 0 to 5, the tensile strain at failure increases by roughly 30-fold to 40-fold (Extended Data Fig. 8l). Furthermore, as ω^* increases from 0 to 3, the Young’s modulus of the filaments decreases by roughly 100-fold (Fig. 4g). As ω^* increases further from 3 to 5, the modulus increases slightly from 9 ± 1 MPa to 31 ± 3 MPa (mean \pm s.d.), which may arise because of an increasing prevalence of an interdiffusion zone^{22,34} between the stiff and soft materials and/or geometric factors in filament deformation as the helical layers become thinner and exhibit a more warped helical architecture. In the extreme case of complete interdiffusion between the stiff and soft acrylic inks within the fan region ($\omega^* \rightarrow \infty$), the filament modulus may be estimated by that of a filament with fully mixed stiff and soft acrylic inks in the fan region and a soft acrylic core (purple line in Fig. 4g). The estimated Young’s modulus for $\omega^* \rightarrow \infty$ is larger than that of the springy filament produced at $\omega^* = 5$, suggesting that it may represent an asymptotic value approached as ω^* increases.

Building on these capabilities, we printed hierarchical 3D lattices in the form of woodpile structures composed of springy filaments. The

lattices are composed of five layers with strut filaments printed in a 0°/90°/0°/90°/0° pattern (Extended Data Fig. 9). Lattices are printed with constant ω^* values of 0, 0.75 and 3, and with a gradient in ω^* ranging from 0 to 3 in the 0° direction (Fig. 4h and Extended Data Fig. 9). All lattices are tested in tension along the 0° direction (Fig. 4i, Extended Data Fig. 10a–c and Supplementary Video 10). Akin to the springy filaments, the moduli of the springy lattices produced at $\omega^* = 0.75$ are roughly an order of magnitude higher than those produced at $\omega^* = 3$ (Extended Data Fig. 10d). Meanwhile, the springy lattices produced using a gradient in ω^* are slightly stiffer than those produced at $\omega^* = 3$, yet reach a similar maximum stress before failure. Furthermore, the lattices with a gradient in ω^* fail in the position along the 0° direction in which $\omega^* \approx 3$, that is, where the lattice is programmed to be weakest, whereas the lattices with ω^* of 0.75 and 3 fail in more random locations (Fig. 4j). Moving forward, we plan to integrate functional materials into these complex architectures.

Summary

We have developed a rotational multimaterial 3D printing method that enables programmable subvoxel control over the local orientation of azimuthally heterogeneous features in multimaterial functional and structural filaments, which can be patterned in 1D, 2D and 3D motifs. By implementing nozzles with more extreme internal features, the resolution, complexity and performance of these hierarchical bioinspired architectures could be further enhanced from the subvoxel scale to the macroscale.

Online content

Any methods, additional references, Nature Portfolio reporting summaries, source data, extended data, supplementary information, acknowledgements, peer review information; details of author contributions and competing interests; and statements of data and code availability are available at <https://doi.org/10.1038/s41586-022-05490-7>.

- Spinks, G. M. Advanced actuator materials powered by biomimetic helical fiber topologies. *Adv. Mater.* **32**, 1904093 (2020).
- Evans, J. J. & Ridge, I. M. L. in *WIT Transactions on State of the Art in Science and Engineering*, Vol. 20 (ed. Jenkins, C. H. M.) Ch. 7, 133–169 (WIT Press, 2005).
- Mu, J. et al. Sheath-run artificial muscles. *Science* **365**, 150–155 (2019).
- Wang, R. et al. Torsional refrigeration by twisted, coiled, and supercoiled fibers. *Science* **366**, 216–221 (2019).
- Yuan, J. et al. Shape memory nanocomposite fibers for untethered high-energy microengines. *Science* **365**, 155–158 (2019).
- Chatterjee, K. & Ghosh, T. K. 3D printing of textiles: potential roadmap to printing with fibers. *Adv. Mater.* **32**, 1902086 (2020).
- Lima, M. D. et al. Electrically, chemically, and photonically powered torsional and tensile actuation of hybrid carbon nanotube yarn muscles. *Science* **338**, 928–932 (2012).
- Xu, P. et al. Bioinspired microfibers with embedded perfusable helical channels. *Adv. Mater.* **29**, 1701664 (2017).
- Yu, Y. et al. Bioinspired helical microfibers from microfluidics. *Adv. Mater.* **29**, 1605765 (2017).
- Kanik, M. et al. Strain-programmable fiber-based artificial muscle. *Science* **365**, 145–150 (2019).
- Huang, M. et al. Nanomechanical architecture of strained bilayer thin films: from design principles to experimental fabrication. *Adv. Mater.* **17**, 2860–2864 (2005).
- Pham, J. T. et al. Highly stretchable nanoparticle helices through geometric asymmetry and surface forces. *Adv. Mater.* **25**, 6703–6708 (2013).
- Wu, Z. L. et al. Three-dimensional shape transformations of hydrogel sheets induced by small-scale modulation of internal stresses. *Nat. Commun.* **4**, 1586 (2013).
- Moestopo, W. P., Mateos, A. J., Fuller, R. M., Greer, J. R. & Portela, C. M. Pushing and pulling on ropes: hierarchical woven materials. *Adv. Sci.* **7**, 2001271 (2020).
- Skylar-Scott, M. A., Gunasekaran, S. & Lewis, J. A. Laser-assisted direct ink writing of planar and 3D metal architectures. *Proc. Natl Acad. Sci.* **113**, 6137–6142 (2016).
- Lebel, L. L., Aissa, B., Khakani, M. A. E. & Theriault, D. Ultraviolet-assisted direct-write fabrication of carbon nanotube/polymer nanocomposite microcoils. *Adv. Mater.* **22**, 592–596 (2010).
- Gladman, A. S., Matsumoto, E. A., Nuzzo, R. G., Mahadevan, L. & Lewis, J. A. Biomimetic 4D printing. *Nat. Mater.* **15**, 413–418 (2016).
- van der Elst, L. et al. 3D printing in fiber-device technology. *Adv. Fiber Mater.* **3**, 59–75 (2021).
- Hart, K. R., Dunn, R. M. & Wetzel, E. D. Tough, additively manufactured structures fabricated with dual-thermoplastic filaments. *Adv. Eng. Mater.* **22**, 1901184 (2020).

20. Loke, G. et al. Structured multimaterial filaments for 3D printing of optoelectronics. *Nat. Commun.* **10**, 4010 (2019).
21. Xu, W. et al. Review of fiber-based three-dimensional printing for applications ranging from nanoscale nanoparticle alignment to macroscale patterning. *ACS Appl. Nano Mater.* **4**, 7538–7562 (2021).
22. Mueller, J., Raney, J. R., Shea, K. & Lewis, J. A. Architected lattices with high stiffness and toughness via multicore-shell 3D printing. *Adv. Mater.* **30**, 1705001 (2018).
23. Chortos, A. et al. Printing reconfigurable bundles of dielectric elastomer fibers. *Adv. Funct. Mater.* **31**, 2010643 (2021).
24. Raney, J. R. et al. Rotational 3D printing of damage-tolerant composites with programmable mechanics. *Proc. Natl Acad. Sci.* **115**, 1198–1203 (2018).
25. Lehman, W., Galińska-Rakoczy, A., Hatch, V., Tobacman, L. S. & Craig, R. Structural basis for the activation of muscle contraction by troponin and tropomyosin. *J. Mol. Biol.* **388**, 673–681 (2009).
26. Armon, S., Efrati, E., Kupferman, R. & Sharon, E. Geometry and mechanics in the opening of chiral seed pods. *Science* **333**, 1726–1730 (2011).
27. Burgert, I. & Fratzl, P. Actuation systems in plants as prototypes for bioinspired devices. *Philos. Trans. R. Soc. A Math. Phys. Eng. Sci.* **367**, 1541–1557 (2009).
28. Reyssat, E. & Mahadevan, L. Hygromorphs: from pine cones to biomimetic bilayers. *J. R. Soc. Interface* **6**, 951–957 (2009).
29. Zhang, J. et al. Robotic artificial muscles: current progress and future perspectives. *IEEE Trans. Robot.* **35**, 761–781 (2019).
30. Carpi, F., Migliore, A., Serra, G. & Rossi, D. D. Helical dielectric elastomer actuators. *Smart Mater. Struct.* **14**, 1210–1216 (2005).
31. Xin, X., Liu, L., Liu, Y. & Leng, J. Pixel mechanical metamaterials with programmable and reconfigurable properties. *Adv. Funct. Mater.* **32**, 2107795 (2022).
32. Lipton, J. I. et al. Handedness in shearing auxetics creates rigid and compliant structures. *Science* **360**, 632–635 (2018).
33. Truby, R. L. & Lewis, J. A. Printing soft matter in three dimensions. *Nature* **540**, 371–378 (2016).
34. Skylar-Scott, M. A., Mueller, J., Visser, C. W. & Lewis, J. A. Voxellated soft matter via multimaterial multinozzle 3D printing. *Nature* **575**, 330–335 (2019).
35. Mahadevan, L., Ryu, W. S. & Samuel, A. D. T. Fluid ‘rope trick’ investigated. *Nature* **392**, 140–140 (1998).
36. Yuk, H. & Zhao, X. A new 3D printing strategy by harnessing deformation, instability, and fracture of viscoelastic inks. *Adv. Mater.* **30**, 1704028 (2018).

Publisher's note Springer Nature remains neutral with regard to jurisdictional claims in published maps and institutional affiliations.

Springer Nature or its licensor (e.g. a society or other partner) holds exclusive rights to this article under a publishing agreement with the author(s) or other rightsholder(s); author self-archiving of the accepted manuscript version of this article is solely governed by the terms of such publishing agreement and applicable law.

© The Author(s), under exclusive licence to Springer Nature Limited 2023

Methods

Materials

The clear PDMS ink was prepared by mixing 170 g of Sylgard 186 base with 17 g of a thiol-functionalized crosslinker ([4–6% (mercaptopyl) methylsiloxane]-dimethylsiloxane copolymer (SMS-042 from Gelest)), 5.61 g of fumed silica (CAB-O-SIL TS-720, Cabot Corp.) and 1.87 g of 2-hydroxy-2-methylpropiophenone (Irgacure 1173) photoinitiator in a SpeedMixer (1,800 rpm, 18 min). The aforementioned clear PDMS inks and all of the following described inks were mixed with a SpeedMixer (FlackTek, Inc.) and 2-min breaks were implemented between every 2 min of mixing to allow time for cooling of the mixer, as recommended by the equipment supplier to increase the mixer lifetime. Red and blue pigmented PDMS inks were prepared by mixing 20 g of the clear PDMS ink with 0.2 g of Silc Pig silicone colour pigment (Smooth-On, Inc.) of the appropriate colour in a SpeedMixer (1,800 rpm, 6 min). The conductive electrode ink used in the HDEA demo was prepared by mixing 40 g of a difunctional aliphatic urethane acrylate oligomer (CN9028, Sartomer) with 24 g of dioctyl phthalate and 8.32 g of carbon black particles (Acetylene Black 50%-01, Soltex, Inc.) in a SpeedMixer (1,800 rpm, 18 min). Carbon black was chosen because of its low density, low cost and good stability³⁷. To improve dispersion of the carbon black, the ink was roll-milled (Torrey Hill, T50) five times. The soft acrylic ink used as both the dielectric elastomer ink in the HDEAs and as the soft structural ink in the springy filaments was prepared by mixing 130 g of urethane acrylate oligomer (CN9018, Sartomer) with 130 g of isodecyl acrylate, 52 g of fumed silica nanoparticles (CAB-O-SIL TS-720, Cabot Corp.) and 2.6 g of 2,2-dimethoxy-2-phenylacetophenone (Irgacure 651) photoinitiator in a SpeedMixer (1,800 rpm, 18 min). To improve dispersion of the silica, the ink was roll-milled (Torrey Hill, T50) five times. The stiff acrylic ink used in the springy filament demo was prepared by mixing 75 g of E-Shell 300 Clear (EnvisionTEC), 6.75 g of fumed silica (CAB-O-SIL M5, Cabot Corp.) and 0.08 g of blue Silc Pig silicone colour pigment (Smooth-On, Inc.) in a SpeedMixer (1,800 rpm, 18 min). The fully mixed stiff and soft acrylic ink referenced in the springy filament discussion (Fig. 4g purple line and Extended Data Fig. 4c) was prepared by mixing the stiff and soft acrylic base materials (described above) in a 50:50 volume ratio in a SpeedMixer (1,800 rpm, 18 min). After preparation, inks were loaded into 55-cc UV/light block amber syringes (Nordson EFD) and centrifuged to remove air bubbles.

Rheological measurements

Rheological measurements on the PDMS ink were performed on a Discovery HR-3 rheometer (TA Instruments) and rheological measurements on the acrylic and carbon-based inks were performed on an AR 2000ex rheometer (TA Instruments). Measurements were performed at 20 °C using a parallel-plate geometry with a diameter of 20 mm and a gap of 0.5 mm. Apparent viscosities were determined by carrying out shear-rate sweeps using shear rates of about 0.01 s⁻¹ to about 100 s⁻¹. Oscillatory measurements were carried out at a frequency of 1 Hz over a range of shear stresses from about 1 Pa to about 1 kPa.

Shell–fan-core nozzles

The shell–fan-core nozzles were designed using 3D computer-aided design software (SolidWorks). The model was printed using a stereolithography 3D printer (Perfactory Aureus, EnvisionTEC). For all nozzles, HTM140_v2 green resin was used, with a layer height of either 25 or 50 μm and a calibrated power of 700 mW. After printing, the nozzles were rinsed with isopropyl alcohol using a wash bottle with a long stem to flush the channels. The nozzles were then dried under a stream of compressed air.

All shell–fan-core nozzles were designed with N_f (integer) regularly spaced identical fans of fan angle ψ (°) with the centreline of the fan walls coinciding with radii of the circular nozzle. The fans are designed with this ‘pizza-slice’ geometry such that the volume fraction of each

material—and thus the axial spacing between material layers—within the fan region is constant with radial position r ($r = 0$ at the core centre). The walls separating the fans from the fan-core and shell (if present) are all 0.1 mm thick at the nozzle tip—the minimum that could be reliably printed on the stereolithography 3D printer. Example nozzle-tip dimensions are illustrated in Extended Data Figs. 1d, 4d and 5d. Ideal filament cross-section dimensions for $Q^* = 1$ assume that extruded inks extend to half of the wall thickness dividing the fans, fan-core and shell (if present) (Extended Data Figs. 1e, 4e and 5e). The desired volumetric flow rates Q_i for each section (such as shell, fan-core and fans) of the nozzle were computed using the area fractions, f_i , of each section of the filament cross-section for an ideal filament with $Q^* = 1$, as well as R and the desired Q^* and v for the given print: $Q_i = (f_i)(Q^*)(v\pi R^2)$.

Rotational multimaterial 3D printing

The shell–fan-core nozzles were attached to ink-filled syringes (Nordson EFD) using short polyurethane tubing with Luer locks on either end, as well as to an XY Linear Stage (M-DS25-XY, Newport Corporation, MKS Instruments, Inc.) for centring the nozzle about the rotation axis. The linear stage was coupled to a long steel shaft (8 mm diameter, 420 Stainless Steel). The steel shaft passed through the central axis of a four-passage rotary union (LT-2141, Dynamic Sealing Technologies, Inc.), was coupled to the shaft of the rotary union (silver part in Fig. 1a) and at its end was coupled to a Nema 17 geared stepper motor (gear ratio 5:1, STEPPERONLINE). Both the rotary union housing (blue part in Fig. 1a) and stepper motor were mounted on an aluminium breadboard (MB1560/M, Thorlabs, Inc.), which was mounted onto a z axis of a 3D motion control system (Aerotech). The stepper motor rotation was synchronized to the print motion through direct interfacing with the 3D motion control system used to translate the printhead in x , y and z directions. Meanwhile, the ink-filled syringes (up to four) were attached to pneumatic couplings (up to four) on the shaft of the rotary union. The four couplings on the shaft of the rotary union connect to four independent fluid passages with corresponding couplings on the housing, allowing for continuous rotation of either component (shaft or housing) and continuous gas flow through the four independent channels. The four pneumatic couplings on the housing of the rotary union were connected to four independent digital pressure controllers (PCD-100PSIG-D, Alicat Scientific), which were used to supply programmed pressures to each of the syringes synchronously with print motion. The pneumatic pressures used for printing were between 0 kPa (0 psi) and 552 kPa (80 psi). The pressure supplied to each independently controlled channel was calibrated individually to achieve the desired volumetric flow rate Q_i of ink from each section (such as shell, fan-core and fans) of the nozzle. Calibration was performed for a given channel and ink by applying a programmed pressure for a programmed amount of time, weighing the quantity of ink extruded during that time and using the extruded ink weight, extrusion time and ink density to compute the volumetric flow rate at the programmed pressure. Pressures were adjusted in an iterative fashion until the pressure corresponding to the desired volumetric flow rate was identified. This process was repeated for each channel and ink. Specific details on the printing methods for the demonstrations using PDMS inks, the HDEA filaments and the springy filaments and lattices are provided in the Supplementary Information.

Mechanical measurements

Springy filaments, consisting of both soft and stiff acrylic, as well as complementary single-material filaments of the soft acrylic (used as both the dielectric elastomer ink in the HDEAs and as the soft structural ink in the springy filaments) and stiff acrylic base materials, and the fully mixed stiff and soft acrylic composition were tested to failure under tension at a rate of 50 mm min⁻¹ with initial gage lengths of about 30 mm (Fig. 4e–g and Extended Data Figs. 4a–c and 8a–k). Springy lattices, consisting of springy filaments composed of both soft and stiff

acrylic, as well as complementary single-material lattices composed of filaments of the soft and stiff acrylic base materials, were also tested to failure under tension at a rate of 50 mm min^{-1} (Fig. 4i, j, Extended Data Fig. 10a–c and Supplementary Video 10). Details on sample preparation, tensile testing, data analysis and computation of the theoretical composite moduli of filaments are provided in the Supplementary Information.

Dielectric constant measurements

The static dielectric constant of the cured soft acrylic ink was obtained by electrochemical impedance spectroscopy. A thin, $97 \pm 11 \text{ }\mu\text{m}$ (mean \pm standard error), film of the dielectric elastomer was blade coated (Gardco Digital Microm Film Applicator) onto a conductive aluminium-coated polyethylene terephthalate substrate. A second electrode was formed on the top surface with gold powder inside a circular, 1-cm-radius, laser-cut acrylic mask with silver-painted edges and copper tape electrical leads. The sample was placed inside a Faraday cage and electrochemical impedance spectroscopy measurements were made with a Gamry Reference 3000 potentiostat and fit using the Python impedance.py package³⁸. A Randles constant phase element (Randles CPE) model³⁹ was found to fit the data better than a resistor in series with a parallel resistor and capacitor (R-(RC)) (Extended Data Fig. 5a). The fit CPE capacitance, C_f , $212 \pm 6 \text{ pF}$ (mean \pm standard error), film thickness (d) and masked area (A_m) are input into the plate capacitor model, $C_f = \epsilon_r \epsilon_0 A_m / d$, to compute the static dielectric constant $\epsilon_r = 7.4 \pm 1.0$ (mean \pm standard error).

The dynamic dielectric constant of the cured soft acrylic ink was obtained by directly measuring the capacitance using the same samples and an Agilent E4980A Precision LCR Meter. The capacitance values were input into the plate capacitor model to compute the dielectric constant ϵ_r (Extended Data Fig. 5b). For the tested capacitance, low-frequency measurements are expected to be of low accuracy owing to device signal noise.

Conductivity measurements

The conductivity of the carbon-black-based conductive electrode ink used in the HDEA application was measured using a Discovery HR 20 rheometer (TA Instruments) equipped with a dielectric accessory and LCR Meter. Measurements were performed at room temperature using a parallel-plate geometry with a diameter of 25 mm. A series equivalent circuit was used. The total conductance, G_T , was measured using an AC signal frequency of 1 kHz and a range of gap heights (distance between parallel plates), g , ranging from 500 μm to 2,000 μm in increments of 100 μm . The total resistance, $R_T = 1/G_T$, is $R_T = (\rho^* g/A_p) + 2R_C + 2R_m$, in which ρ is the resistivity of the ink, A_p is the area of the parallel plate, R_C is the contact resistance and R_m is the resistance of the contact metal. Thus, the slope of a plot of R_T versus g is equal to ρ/A_p . Linear regression of R_T versus g gives a slope, ρ/A_p , of 260,000 ohm m^{-1} with a standard error of 54,000 ohm m^{-1} (Extended Data Fig. 5c). Thus, the resistivity of the ink $\rho = 130 \pm 30 \text{ ohm}\cdot\text{m}$ (mean \pm standard error) and the conductivity, $\sigma = 1/\rho$, is $8 \times 10^{-3} \pm 2 \times 10^{-3} \text{ S m}^{-1}$ (mean \pm standard error) at 1 kHz.

HDEA filament actuation

HDEA filaments were prepared for testing by removing the tips of the initial and final segments (in which $\omega^* = 0$), inserting silver-plated copper wires into the electrode fans approximately 1 cm deep into the final segment section of the filament and then encapsulating the exposed ends in the soft acrylic ink. For strain and twist measurements using image analysis, a subset of the HDEA specimens were coated with a white speckle pattern by means of a spray paint (Rust-Oleum) mist. Other specimens were left bare. The HDEAs were then attached to a frame and allowed to hang freely. Two alligator clips were attached to

the wires: one clip for the two positive electrodes and one clip for the two negative electrodes. A LabVIEW program was used to apply sine wave voltage profiles (XP Power CB101 high-voltage power supply, 10 kV maximum output voltage) while recording video of the HDEA actuation from the side and bottom of the filament using two uEye cameras (IDS Imaging Development Systems Inc.) (Extended Data Fig. 7). The sine wave voltage profiles had a minimum voltage of 0 kV and a maximum voltage that was increased incrementally until device breakdown or up to 10 kV (the maximum of the power supply). Further details on sample preparation, voltage profiles, image analysis for axial strain and twist measurements, and estimation of breakdown fields are provided in the Supplementary Information.

Analytical modelling of HDEAs

A previously unpublished approximate analytical expression for the axial actuation strain of an HDEA predicts that the strain varies as the voltage squared and that the geometrical characteristics are embodied in a dependence on $\phi(r)$. Comparison with the finite element simulations shows that the simple analytical model is reasonably successful in capturing the helical geometry but also supports the necessity of the detailed electromechanical simulations. The details and derivation of the analytical expression are provided in the Supplementary Information.

Finite element simulations of HDEAs

The commercial finite element software COMSOL Multiphysics 5.5 (Dassault Systèmes, Waltham, MA, USA) was used to numerically investigate the response of the HDEA filaments. Further details are provided in the Supplementary Information.

Data availability

The main data supporting the findings of this study are available within the paper and its Supplementary Information. Other datasets generated or analysed during the current study are available from the corresponding author on request. Source data are provided with this paper.

37. Chortos, A., Hajiesmaili, E., Morales, J., Clarke, D. R. & Lewis, J. A. 3D printing of interdigitated dielectric elastomer actuators. *Adv. Funct. Mater.* **30**, 1907375 (2020).
38. Murbach, M., Gerwe, B., Dawson-Elli, N. & Tsui, L. impedance.py: a Python package for electrochemical impedance analysis. *J. Open Source Softw.* **5**, 2349 (2020).
39. Lasia, A. *Electrochemical Impedance Spectroscopy and its Applications* (Springer, 2014).

Acknowledgements We gratefully acknowledge support from the National Science Foundation under the Materials Research Science and Engineering Centers (DMR-2011754), National Science Foundation Designing Materials to Revolutionize and Engineer our Future (DMREF-15-33985), the Vannevar Bush Faculty Fellowship Program, sponsored by the Basic Research Office for the Assistant Secretary of Defense for Research and Engineering through the Office of Naval Research grant N00014-21-1-2958, and the GETTYLAB. We thank L. K. Sanders for assistance with photography and videography, J. W. Williams for assistance with the Python image analysis pipeline and E. Hajiesmaili, N. Colella, M. Kolloosche, S. G. M. Uzel, A. Kotikian, R. D. Weeks, D. Kokkinis, D. Barber, E. Davidson, D. Foresti and E. Guzman for experimental assistance and helpful discussions.

Author contributions N.M.L., J.M., A.C., Z.S.D. and J.A.L. designed the research. N.M.L., J.M., A.C. and Z.S.D. performed the research. N.M.L., J.M., A.C., Z.S.D. and D.R.C. analysed the data. N.M.L., J.M., A.C., Z.S.D., D.R.C. and J.A.L. prepared the manuscript.

Competing interests A US patent has been filed by Harvard University on this research. J.A.L. serves on Advisory Boards for Autodesk, Azul 3D, and Desktop Health (a subsidiary of Desktop Metal, Inc.).

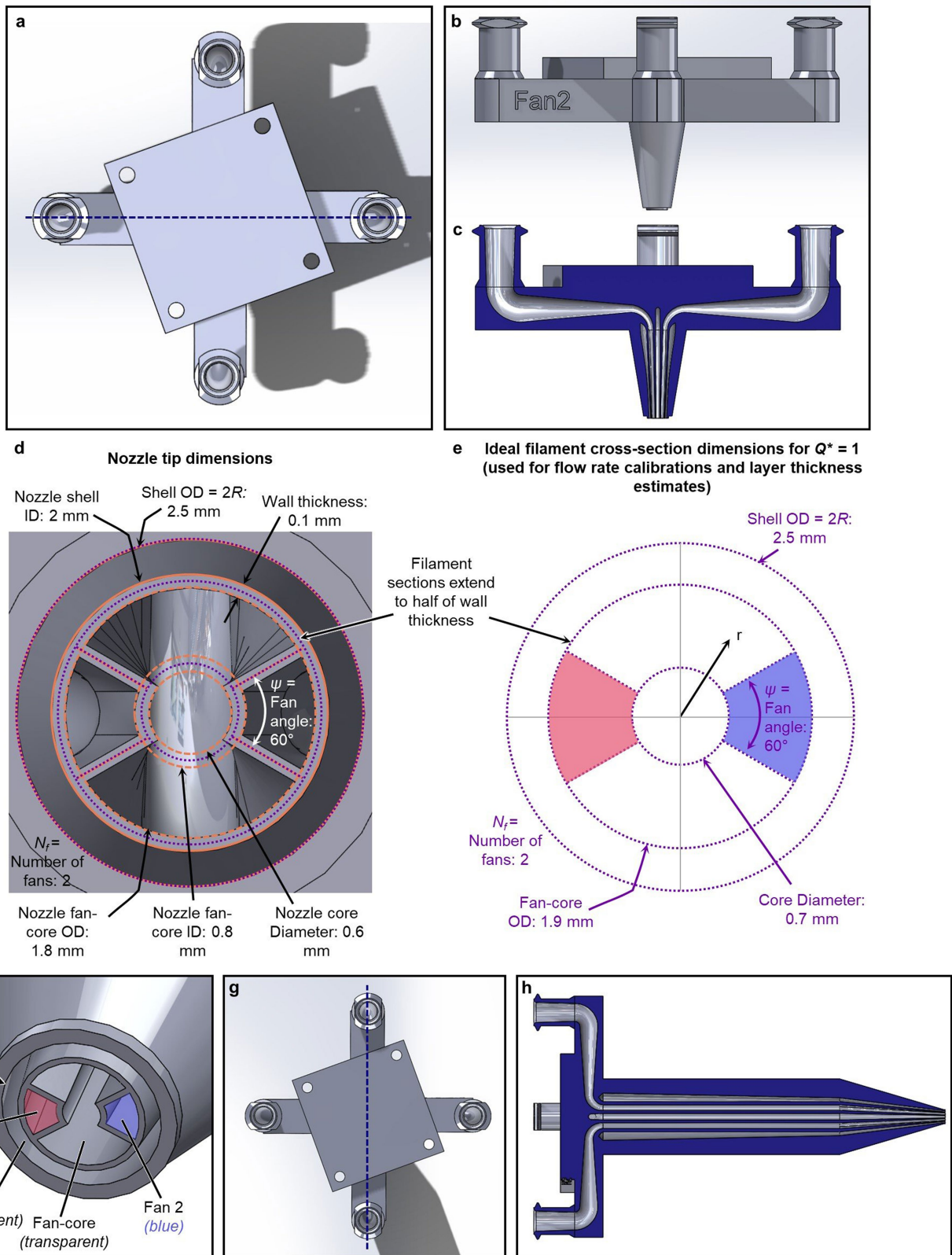
Additional information

Supplementary information The online version contains supplementary material available at <https://doi.org/10.1038/s41586-022-05490-7>.

Correspondence and requests for materials should be addressed to Jennifer A. Lewis.

Peer review information Nature thanks Brittany Newell and the other, anonymous, reviewer(s) for their contribution to the peer review of this work.

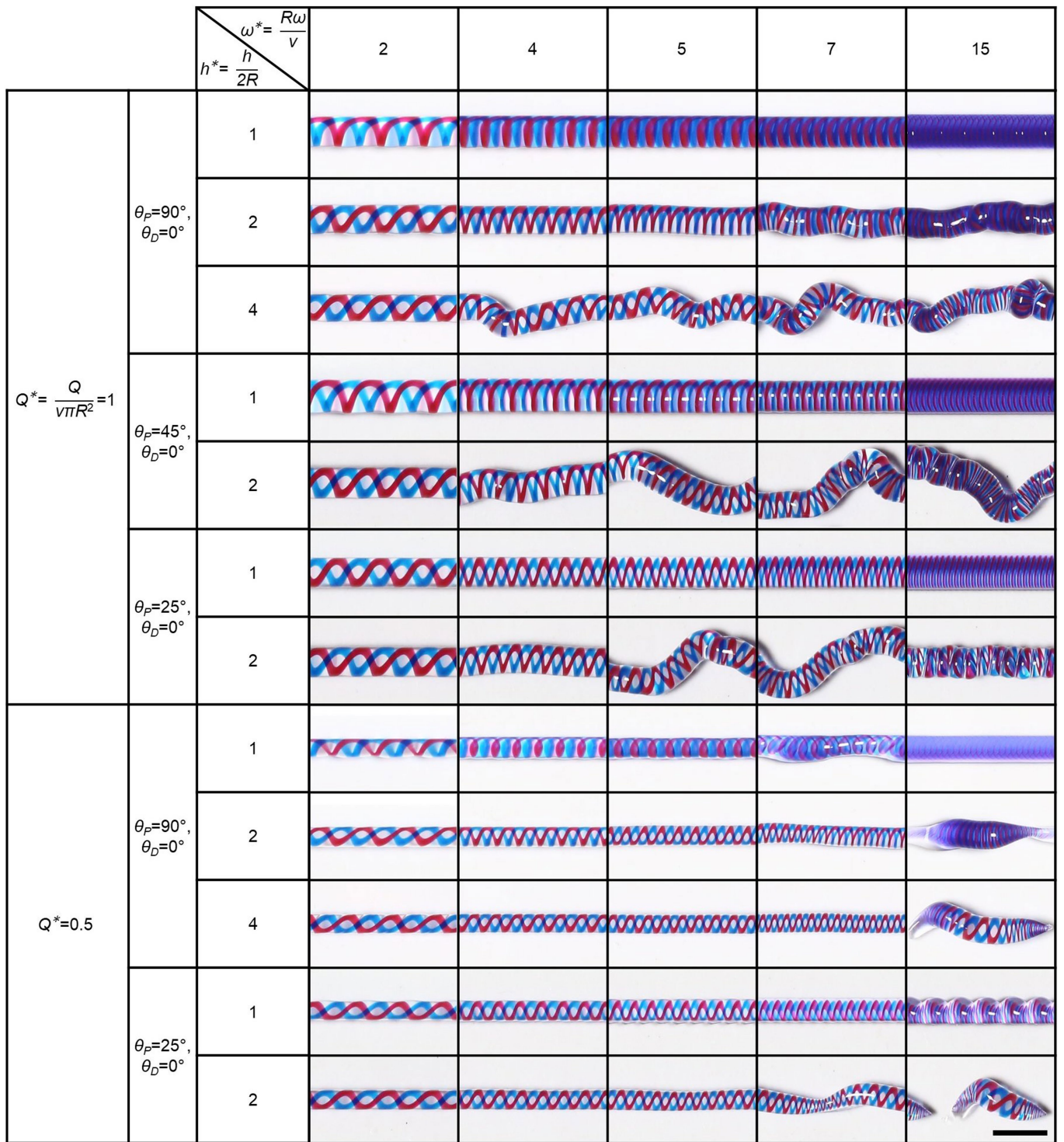
Reprints and permissions information is available at <http://www.nature.com/reprints>.



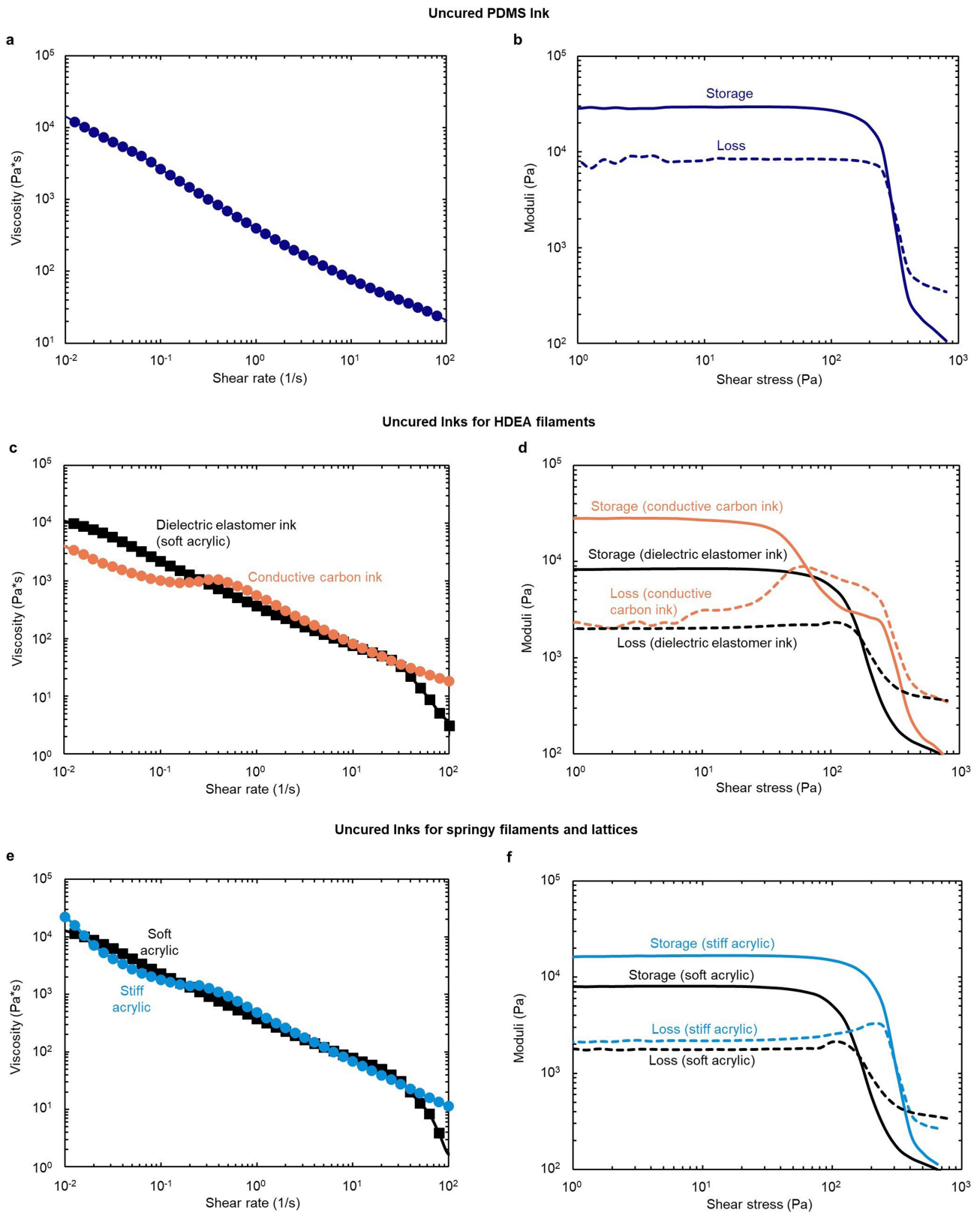
Extended Data Fig. 1 | See next page for caption.

Extended Data Fig. 1 | Shell-fan-core nozzle used for RM-3DP of PDMS inks. **a–e**, Nozzle for RM-3DP in the prototypical printing configuration ($\theta_p = 90^\circ$, $\theta_d = 0^\circ$). **a**, Top view of 3D model of entire nozzle showing four Luer lock fittings for connecting to syringes and square mounting component for coupling to centring stage. **b**, Side view of 3D model of entire nozzle. **c**, Section view of 3D model of entire nozzle from same viewing direction as **b**, with section taken along the dashed line in **a**. **d**, Dimensions of nozzle tip overlaid on 3D model of nozzle tip. ID, inner diameter; OD, outer diameter. **e**, Ideal filament cross-section dimensions for $Q^* = 1$ assume extruded inks extend to half of the wall

thickness, dividing the fans from the fan-core and shell. These dimensions were used to calibrate volumetric flow rates before printing. **f–h**, Various views of 3D model of long shell-fan-core nozzle for RM-3DP in the angled printing configuration ($\theta_p < 90^\circ$, $\theta_d = 0^\circ$). Nozzle-tip dimensions and estimated filament cross-section dimensions are identical to those of the shorter nozzle illustrated in **a–e**. **f**, 3D model of tip geometry. **g**, Top view of 3D model of entire nozzle. **h**, Section view of 3D model of entire nozzle, with section taken along the dashed line in **g**.

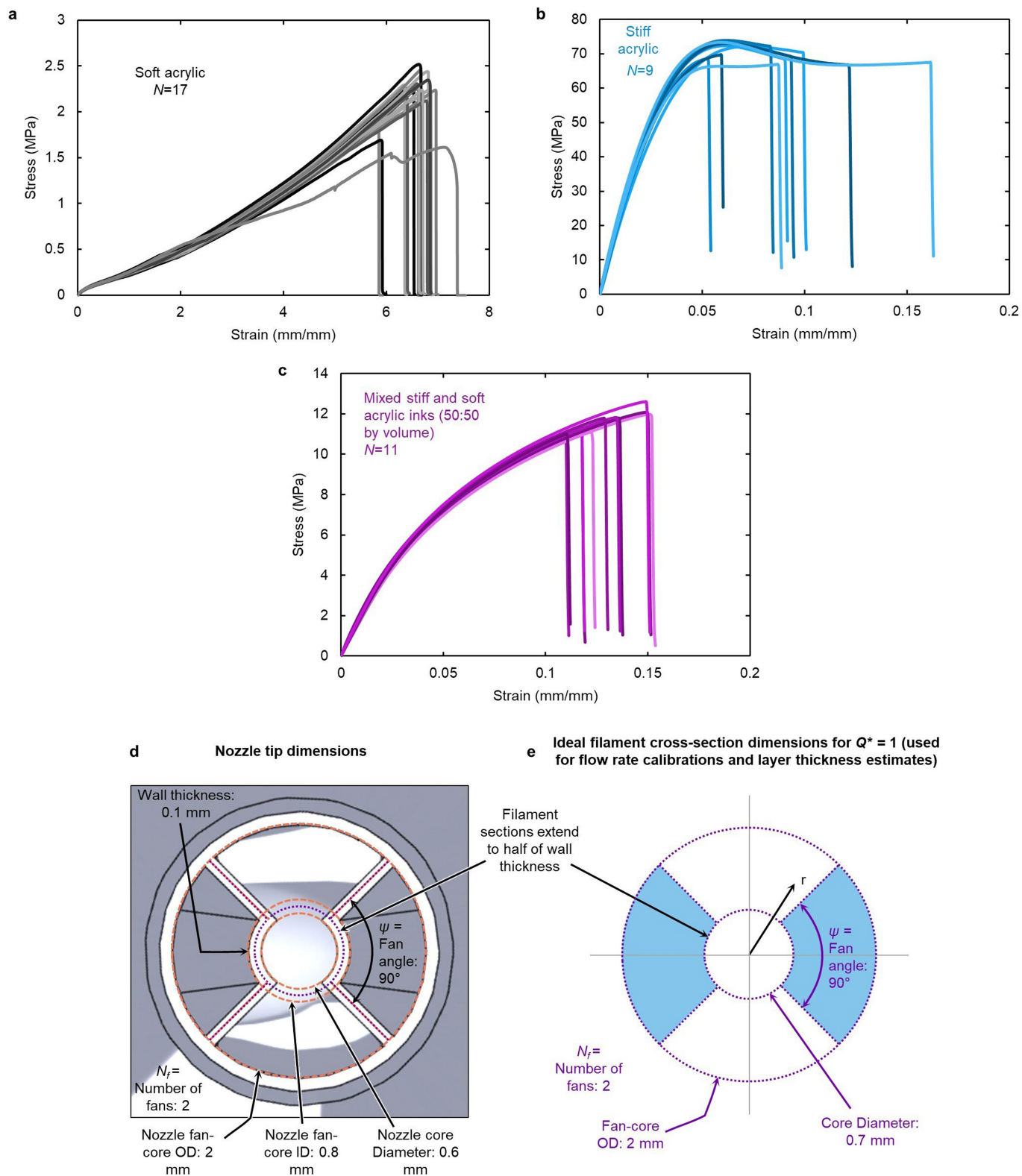


Extended Data Fig. 2 | Effects of printing configuration and printing parameters on PDMS filament and subvoxel geometry. PDMS filaments were extruded from shell-fan-core nozzles presented in Fig. 1b and Extended Data Fig. 1. Scale bar: 5 mm.



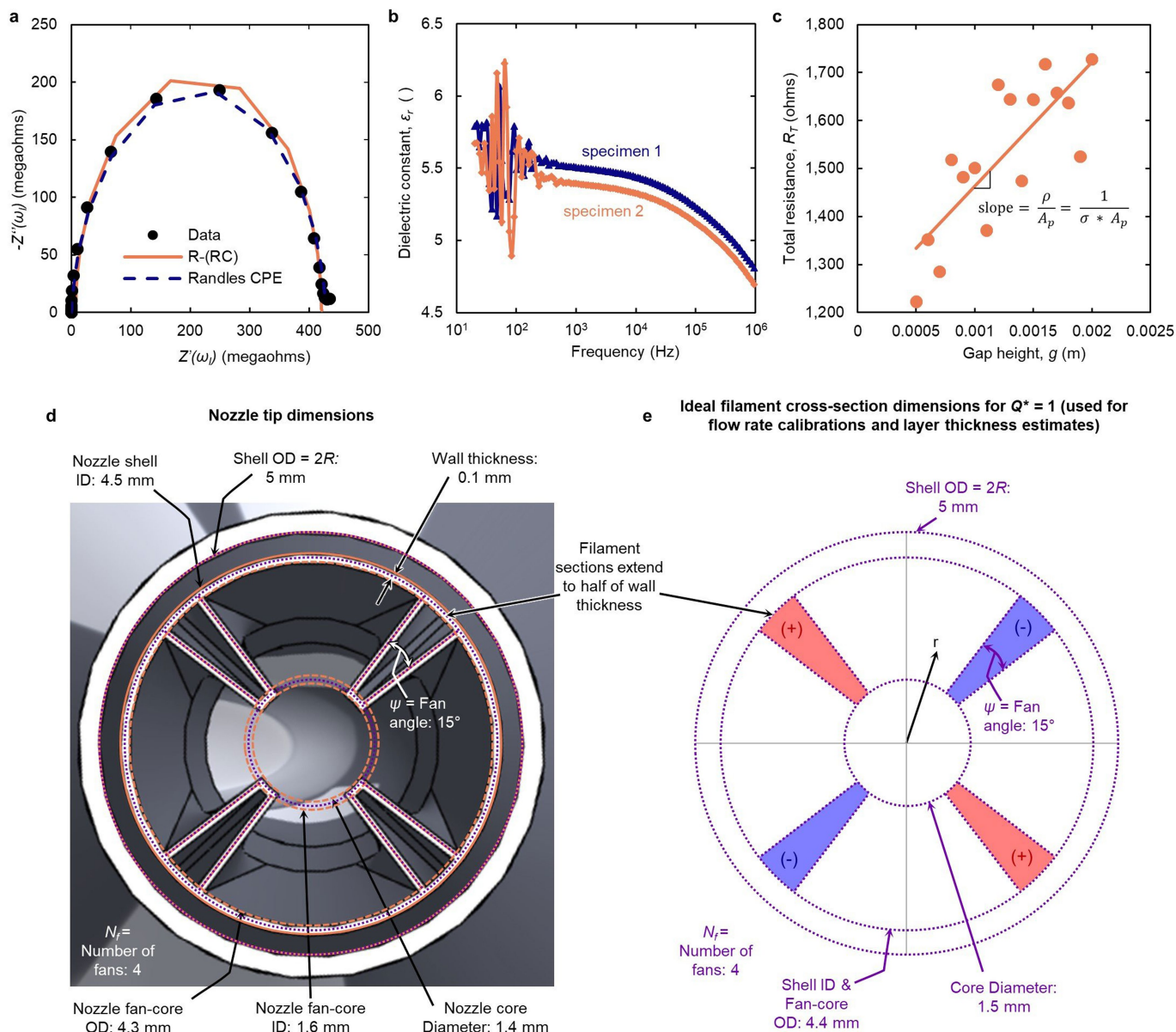
Extended Data Fig. 3 | Rheological properties of printable inks. Log-log plots of the apparent viscosity as a function of shear rate (a,c,e) and the shear moduli as a function of shear stress (b,d,f) for the uncured PDMS ink (a,b), the

uncured dielectric elastomer and conductive carbon inks for HDEA filaments (c,d) and the uncured soft acrylic and stiff acrylic inks for springy filaments and lattices (e,f).



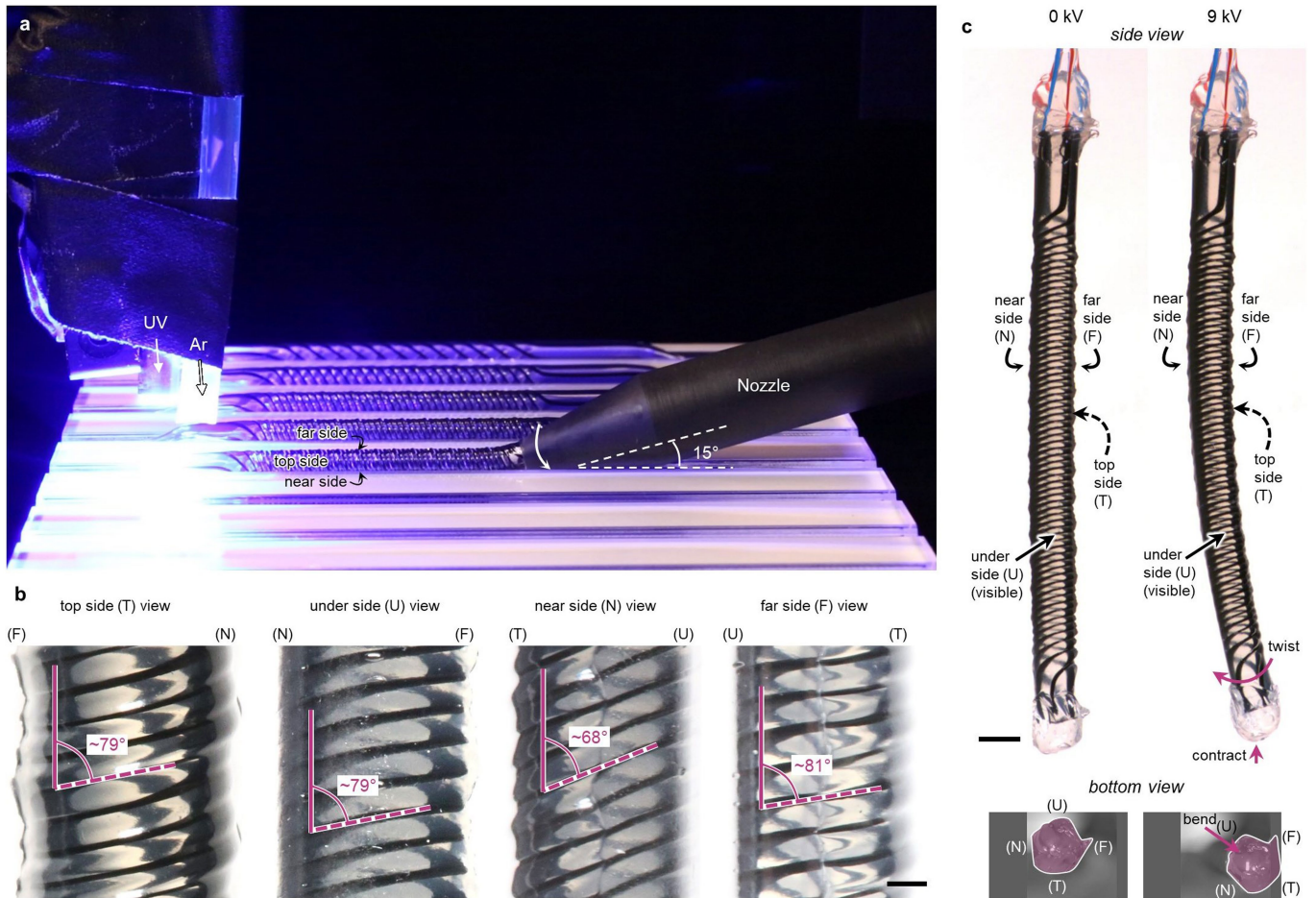
Extended Data Fig. 4 | Materials and nozzle geometry for springy filaments and lattices. a–c, Tensile testing of cured soft, stiff and mixed acrylic base materials. **a,** Stress–strain curves for $N=17$ tensile tests for cured soft acrylic (Young’s modulus = 0.52 ± 0.03 MPa; mean \pm s.d.), used as both the dielectric elastomer ink in the HDEAs and as the soft structural ink in the springy filaments. **b,** Stress–strain curves for $N=9$ tensile tests for cured stiff acrylic (Young’s modulus = $2,700 \pm 200$ MPa; mean \pm s.d.). **c,** Stress–strain curves for

$N=11$ tensile tests for a fully mixed combination of the stiff and soft acrylic base materials in a 50:50 volume ratio (Young’s modulus = 220 ± 20 MPa; mean \pm s.d.). **d,e,** Fan-core geometry used in RM-3DP of springy filaments and lattices. **d,** Dimensions of nozzle tip overlaid on 3D model of nozzle tip. **e,** Ideal filament cross-section dimensions for $Q^* = 1$ assume extruded inks extend to half of the wall thickness, dividing the fans from the fan-core. These dimensions were used to calibrate volumetric flow rates before printing.



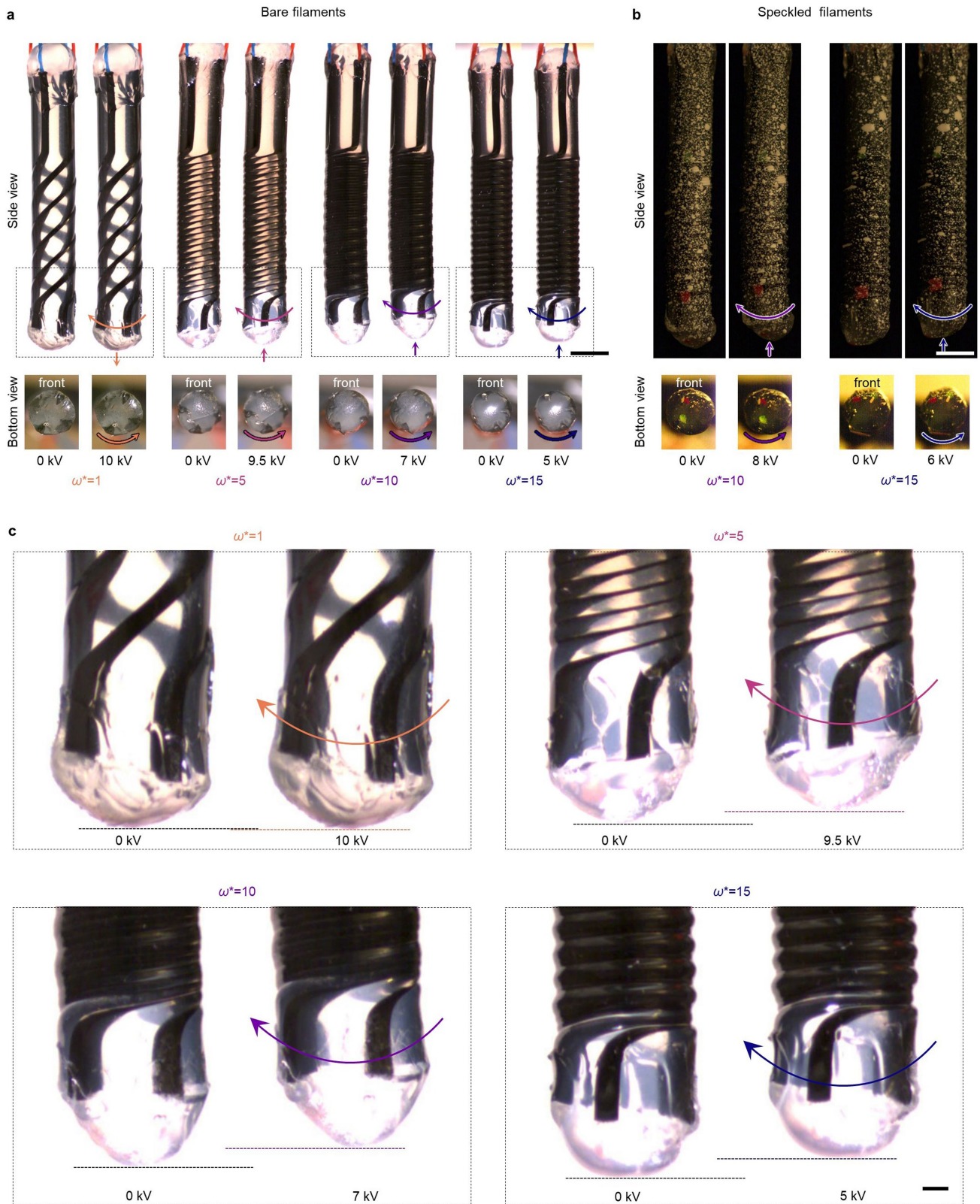
Extended Data Fig. 5 | Material properties and nozzle geometry for HDEA filaments. **a, b.** Dielectric constant of crosslinked dielectric elastomer ink. **a.** Static dielectric constant measurements. A Randles CPE model was found to fit the data better than a resistor in series with a parallel resistor and capacitor (R-(RC)). **b.** Dynamic dielectric constant for two specimens. For each specimen, capacitance measurements were performed three times. The plotted data points represent the average dielectric constant computed from the three measurements. For the tested capacitance, low-frequency measurements are expected to be of low accuracy owing to device signal noise. **c.** Conductivity measurement of carbon-black-based conductive electrode ink. Plot of total resistance, R_T , versus gap height, g , using an AC signal frequency of 1 kHz.

Linear regression of R_T versus g gives a slope, ρ/A_p , of $260,000 \text{ ohm m}^{-1}$ with a standard error of $54,000 \text{ ohm m}^{-1}$, in which ρ is the resistivity of the ink and A_p is the area of the parallel plate. Thus, the resistivity of the ink $\rho = 130 \pm 30 \text{ ohm}\cdot\text{m}$ (mean \pm standard error) and the conductivity, $\sigma = 1/\rho$, is $8 \times 10^{-3} \pm 2 \times 10^{-3} \text{ S m}^{-1}$ (mean \pm standard error). **d, e.** Shell-fan-core geometry for RM-3DP of HDEAs. **d.** Dimensions of nozzle tip overlaid on 3D model of nozzle tip. **e.** Ideal filament cross-section dimensions for $Q^* = 1$ assume extruded inks extend to half of the wall thickness, dividing the fans from the fan-core and shell. These dimensions were used to calibrate volumetric flow rates before printing, to compute dielectric layer thicknesses and to create filament geometries for finite element analysis simulations.



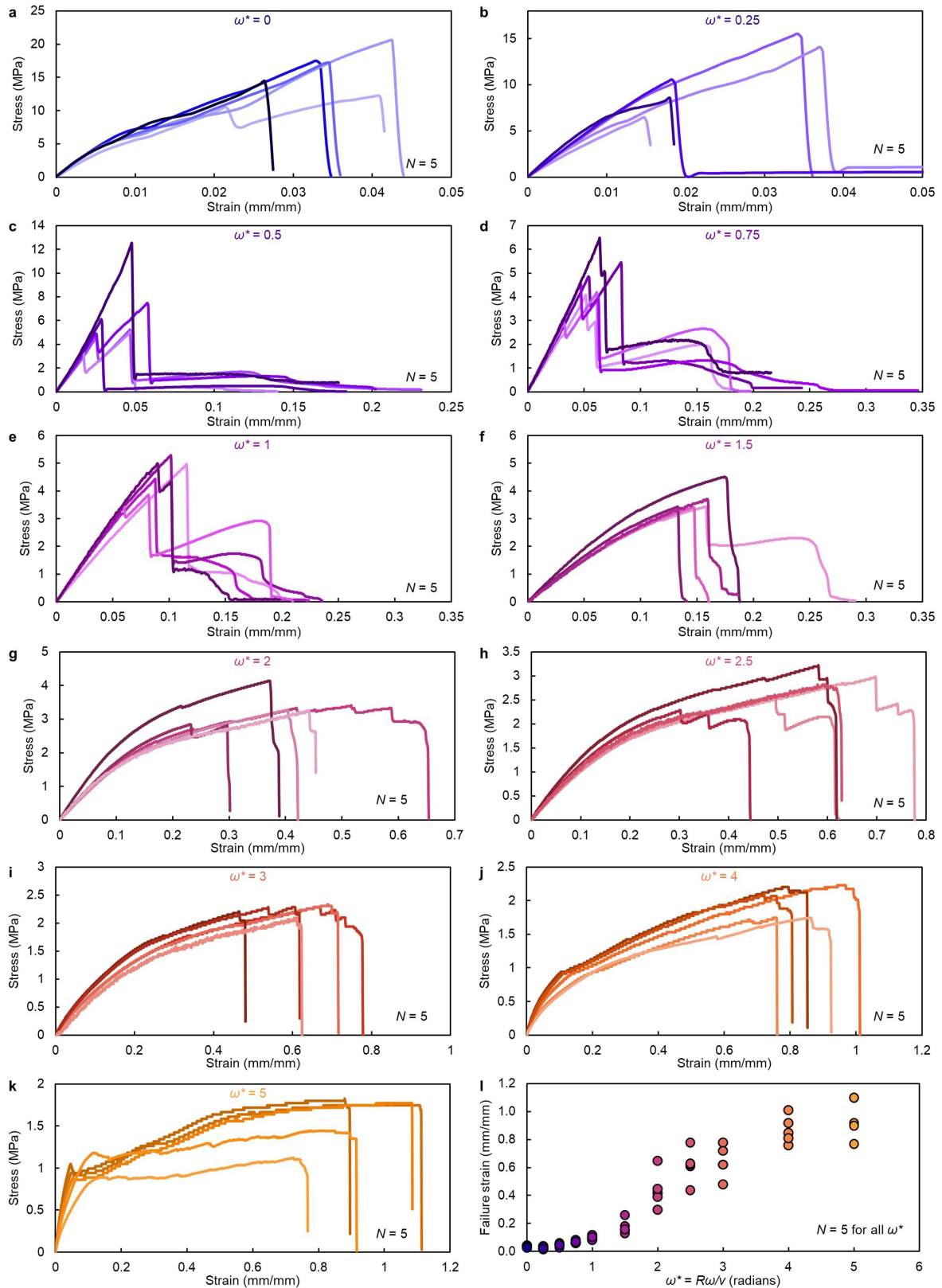
Extended Data Fig. 6 | HDEAs fabricated with printhead at an angle and deposition surface oriented horizontally. **a**, Photograph of HDEA filament deposition with UV curing on the fly. The filament being printed in the photograph has $\omega^* = 5$. The top, near and far sides of the filament are labelled for reference for the following images. **b**, Microscope images showing the top, under, near and far sides of a filament with $\omega^* = 5$, showing the warping of the helical architecture. The angle of the helical features on the outer surface on

the far side (about 81°) is notably higher than that on the near side (about 68°). Also note that the filament surface on the top side is slightly bumpy, whereas the surface on the underside is relatively smooth. Scale bar: 1 mm. **c**, Photograph of actuation of an HDEA with $\omega^* = 5$, showing the filament at 0 kV and 9 kV applied voltages. The filament contracts slightly in the axial direction, twists in the direction that tightens the helix and bends towards the far and top sides. Scale bar: 5 mm.

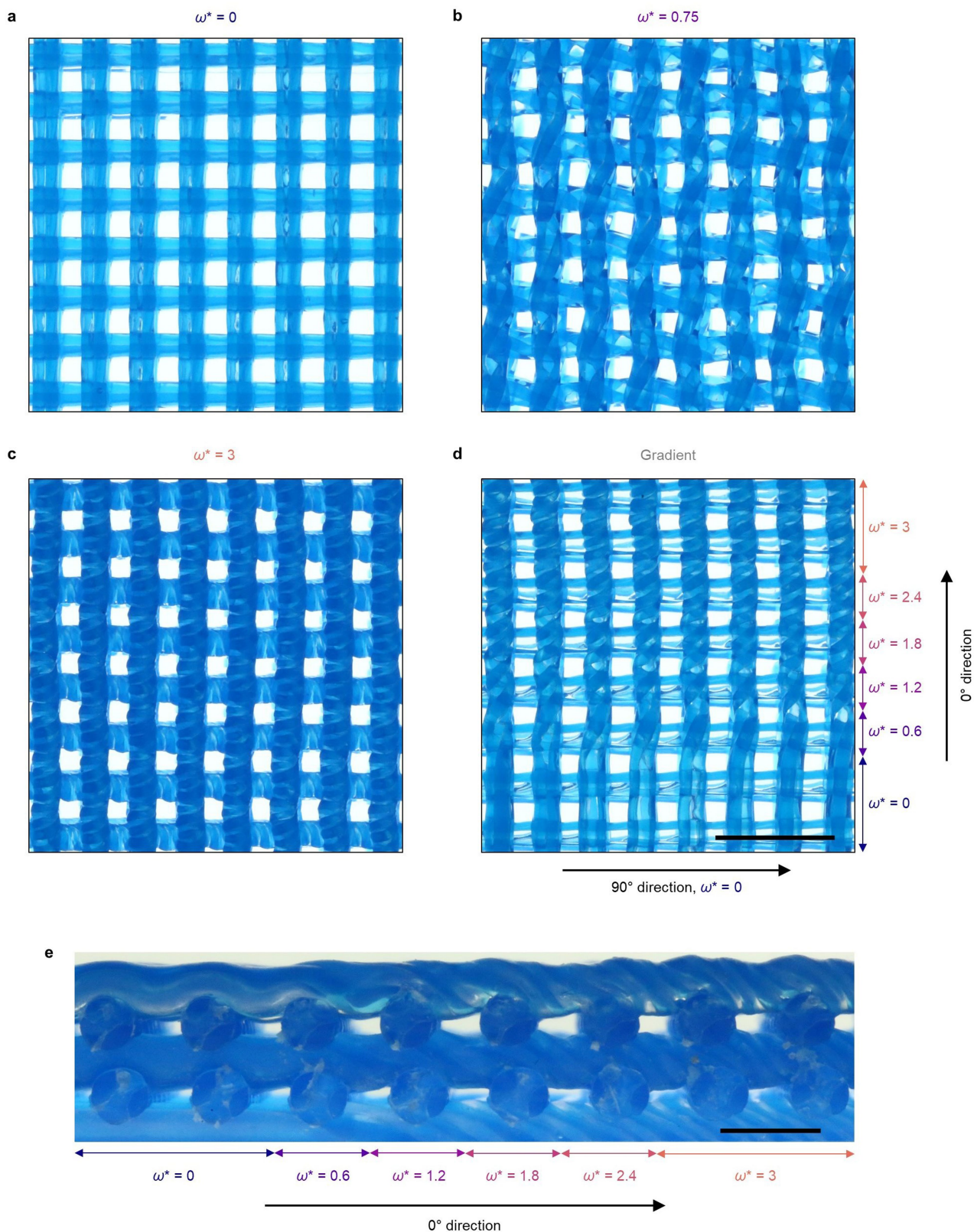


Extended Data Fig. 7 | Actuation of HDEAs printed in the vertical configuration ($\theta_p = 90^\circ, \theta_b = 90^\circ$). Photographs of side views and bottom views of several HDEAs before actuation (0 kV) and during actuation (>0 kV), showing filament twisting and axial extension ($\omega^* = 1$) or contraction ($\omega^* = 5, 10$ and 15).

Examples of both bare filaments (a) and speckled filaments (b) (for twist and axial strain measurements) are shown. Scale bars in a and b: 5 mm. In c, magnified views of the filaments in a are provided. Scale bar: 1 mm.

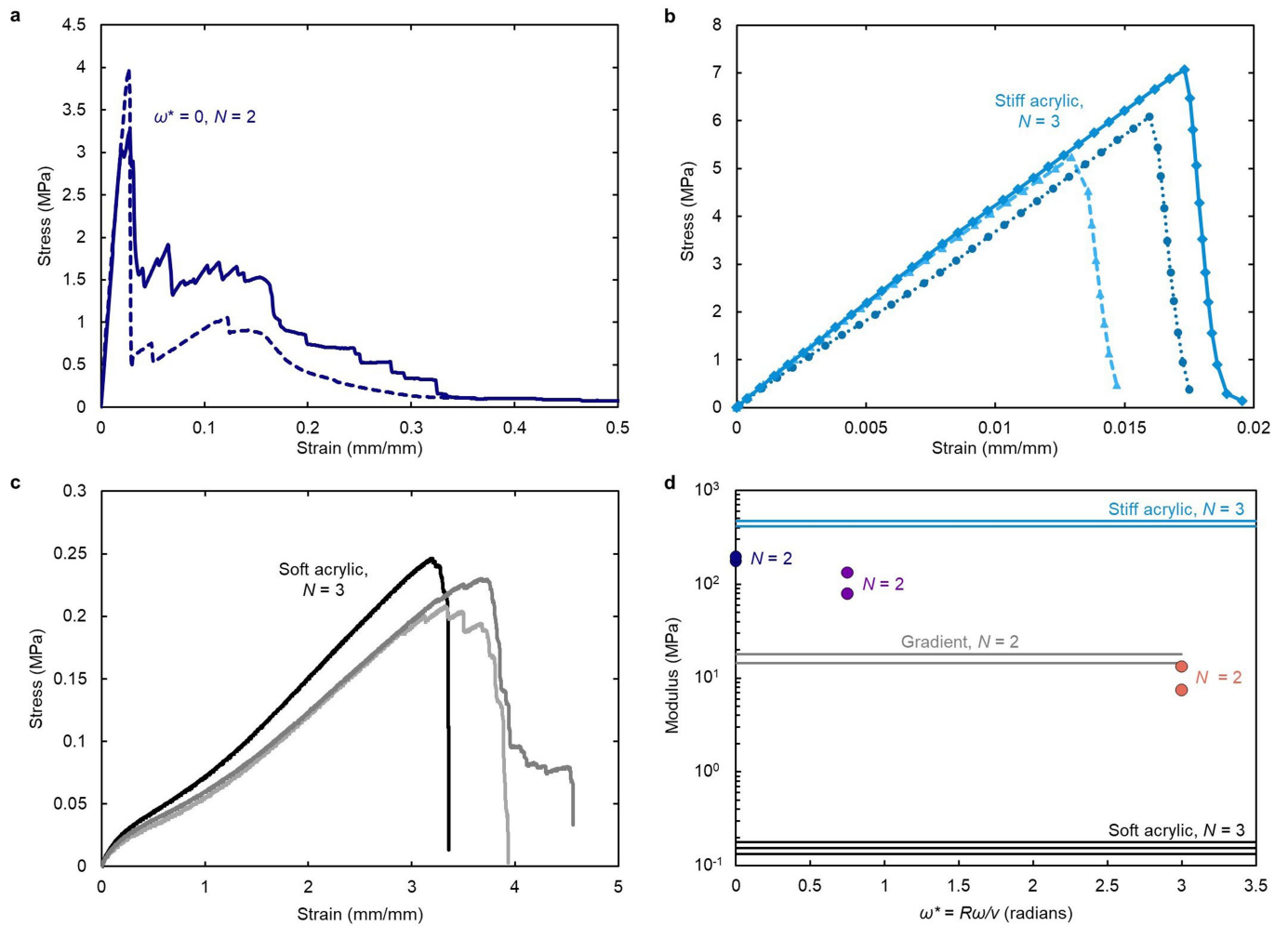


Extended Data Fig. 8 | Tensile measurements on springy filaments. a–k, Stress–strain curves for springy filaments with ω^* ranging from 0 to 5 ($N = 5$ for all). **l,** Failure strain of springy filaments as a function of ω^* .



Extended Data Fig. 9 | Springy 3D lattices. a–d, Photographs of springy lattices composed of filaments with $\omega^* = 0$ (a), $\omega^* = 0.75$ (b), $\omega^* = 3$ (c) and a gradient in ω^* ranging from 0 to 3 in the 0° direction and $\omega^* = 0$ in the 90° direction (d). Scale bar: 10 mm. e, Image of one of the cut faces of a springy

lattice with a gradient in ω^* in the 0° direction. The spanning of the filaments across gaps in the woodpile lattice results in slightly wavy, rather than straight, filaments within the structure. The wavy nature of the filaments is expected to influence the mechanical properties of the lattices. Scale bar: 4 mm.



Extended Data Fig. 10 | Tensile measurements on 3D lattices. a–c, Stress–strain curves for springy lattices composed of filaments with $\omega^* = 0$ ($N = 2$) (a), lattices composed of only stiff acrylic filaments ($N = 3$) (b) and lattices composed of only soft acrylic filaments ($N = 3$) (c). **d,** Moduli of springy lattices as a function of ω^* ($N = 2$ for each ω^*). Solid grey lines are the moduli of the

springy lattices with a gradient in ω^* in the 0° direction ($N = 2$), solid blue lines are the moduli of the lattices composed of pure stiff acrylic filaments ($N = 3$) and solid black lines are the moduli of the lattices composed of pure soft acrylic filaments ($N = 3$).